

# Asthenospheric low-velocity zone consistent with globally prevalent partial melting

Received: 17 April 2022

Accepted: 13 December 2022

Published online: 6 February 2023

 Check for updates

Junlin Hua  <sup>1,2</sup>, Karen M. Fischer  <sup>1</sup>, Thorsten W. Becker  <sup>2,3,4</sup>, Esteban Gazel  <sup>5</sup> & Greg Hirth<sup>1</sup>

The asthenosphere plays a fundamental role in present-day plate tectonics as its low viscosity controls how convection in the mantle below it is expressed at the Earth's surface above. The origin of the asthenosphere, including the role of partial melting in reducing its viscosity and facilitating deformation, remains unclear. Here we analysed receiver-function data from globally distributed seismic stations to image the lower reaches of the asthenospheric low-seismic-velocity zone. We present globally widespread evidence for a positive seismic-velocity gradient at depths of ~150 km, which represents the base of a particularly low-velocity zone within the asthenosphere. This boundary is most commonly detected in regions with elevated upper-mantle temperatures and is best modelled as the base of a partially molten layer. The presence of the boundary showed no correlation with radial seismic anisotropy, which represents accumulated mantle strain, indicating that the inferred partial melt has no substantial effect on the large-scale viscosity of the asthenosphere. These results imply the presence of a globally extensive, partially molten zone embedded within the asthenosphere, but that low asthenospheric viscosity is controlled primarily by gradual pressure and temperature variations with depth.

The asthenosphere, the low-viscosity mantle layer that separates the relatively rigid lithosphere from the deeper mantle, not only facilitates plate tectonics by accommodating plate motions with respect to the deeper mantle, but may also help to stabilize the very existence of tectonic plates in their present-day form<sup>1</sup>. The asthenosphere is characterized by low seismic velocities<sup>2</sup> and strong seismic anisotropy<sup>2–5</sup>. While temperature and pressure variations with depth contribute to creating low-velocity and low-viscosity asthenosphere<sup>6</sup>, the distribution and effects of partial melt remain debated. Some analyses of geophysical data have indicated that partial melt is present and lowers viscosity in the asthenosphere over broad regions of Earth<sup>7–11</sup>, while others suggest that partial melt is not required to explain the low viscosity or even the low seismic velocity within the asthenosphere<sup>6,12–14</sup>. To fundamentally understand the origins of the low-viscosity asthenosphere, resolving

the global distribution of partial melt, both laterally and vertically, is required.

Despite many investigations of the asthenospheric low-seismic-velocity zone (LVZ), its lower boundary has remained particularly unclear. With the use of reflected and converted seismic waves, a negative seismic-velocity gradient with depth (NVG) marking the top of the LVZ has been detected in many regions<sup>5,9,15–18</sup>. However, only a small number of scattered wave studies<sup>17–20</sup> have imaged the positive velocity gradient (PVG) at the base of the LVZ, and the PVG measured by surface waves<sup>2,4,5,14</sup> is not sufficiently well resolved in depth to determine its relationship to mantle melting processes.

To address this problem, we analysed Sp scattered seismic waves to image the lower reaches of the asthenospheric LVZ, finding a significant vertically localized PVG at depths of approximately 150 km that

<sup>1</sup>Department of Earth, Environmental and Planetary Sciences, Brown University, Providence, RI, USA. <sup>2</sup>Department of Geological Sciences, Jackson School of Geosciences, The University of Texas at Austin, Austin, TX, USA. <sup>3</sup>Institute for Geophysics, Jackson School of Geosciences, The University of Texas at Austin, Austin, TX, USA. <sup>4</sup>Oden Institute for Computational Engineering and Sciences, The University of Texas at Austin, Austin, TX, USA.

<sup>5</sup>Department of Earth and Atmospheric Sciences, Cornell University, Ithaca, NY, USA.  e-mail: [junlin.hua@austin.utexas.edu](mailto:junlin.hua@austin.utexas.edu)

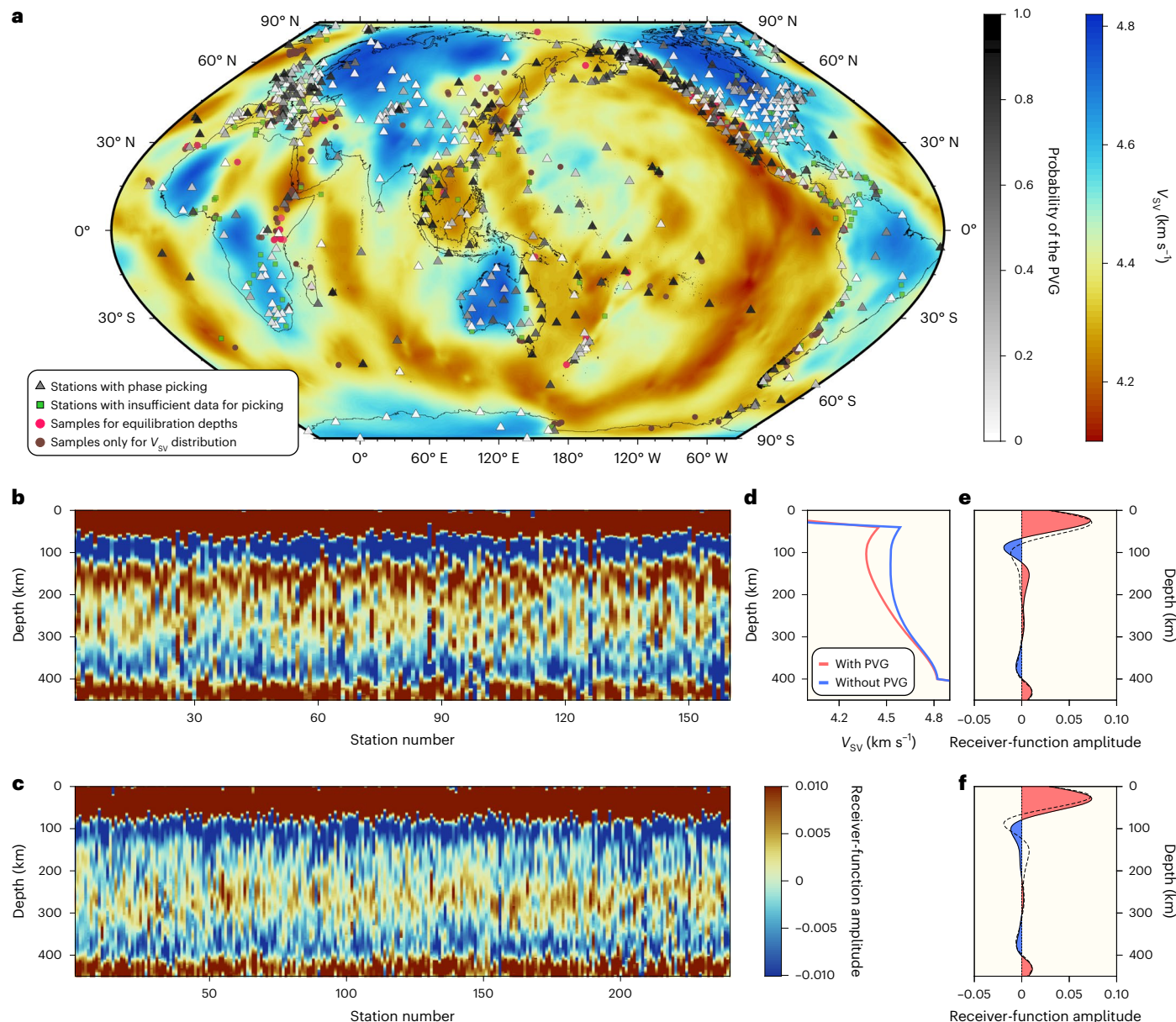


**Fig. 1 | Globally distributed receiver functions.** **a**, Stations shaded by PVG-150 probability (triangles) or without sufficient data for probability quantification (squares). Background shows average  $V_{sv}$  at 110–130 km depths<sup>22</sup>. Dots are basalt samples used for distributions of melt equilibration depths (Fig. 3d) and sample  $V_{sv}$  (Fig. 3d inset). **b,c**, Sp receiver functions for single stations with (**b**) and

without (**c**) the PVG-150. Red phases represent PVGs; blue are NVGs. **d**, Average  $V_{sv}$  profiles for stations with/without ( $P > 80\% / P < 20\%$ ) the PVG-150. **e,f**, Receiver-function sums from stations with (**e**) and without (**f**) the PVG-150. Dashed line in **e** is the sum in **f**, and vice versa.

is widely distributed globally where upper-mantle temperatures are elevated. This PVG can be modelled as the base of an asthenospheric layer containing partial melt. However, the presence of this PVG does not correlate with higher asthenospheric strain as expressed in seismic anisotropy, indicating that while the partial melt in the LVZ reduces seismic velocities, it does not dramatically lower viscosities.

### Imaging the asthenospheric LVZ

We constrained the boundaries of the asthenospheric LVZ using globally distributed Sp receiver functions. When a body wave encounters an impedance contrast, scattered waves are generated, and receiver functions can be calculated by deconvolving the incident wave from the scattered wave to extract information about the depth and velocity gradient of the contrast. Sp receiver functions, which represent

scattered P waves in response to an incident S wave, are especially useful to image upper-mantle discontinuities since they are not influenced by crustal reverberations that affect Ps receiver functions<sup>15</sup> (Supplementary Method 1). We collected data from 716 permanent stations (Fig. 1a). After quality control, 184,340 individual Sp receiver functions remained, which were migrated to depth and, at each station, stacked to represent Earth structure (Methods).

The probabilities,  $P$ , that shear-wave velocity contrasts at the top and the bottom of the LVZ exist were estimated from the receiver functions (Fig. 1, Extended Data Fig. 1 and Methods). A shallow mantle NVG that is consistent with the depth range of the seismic lithosphere-asthenosphere boundary (LAB) inferred from global tomography<sup>21,22</sup> is found at most non-cratonic stations, marking the top boundary of the LVZ. At depths typically near 150 km, conversions from

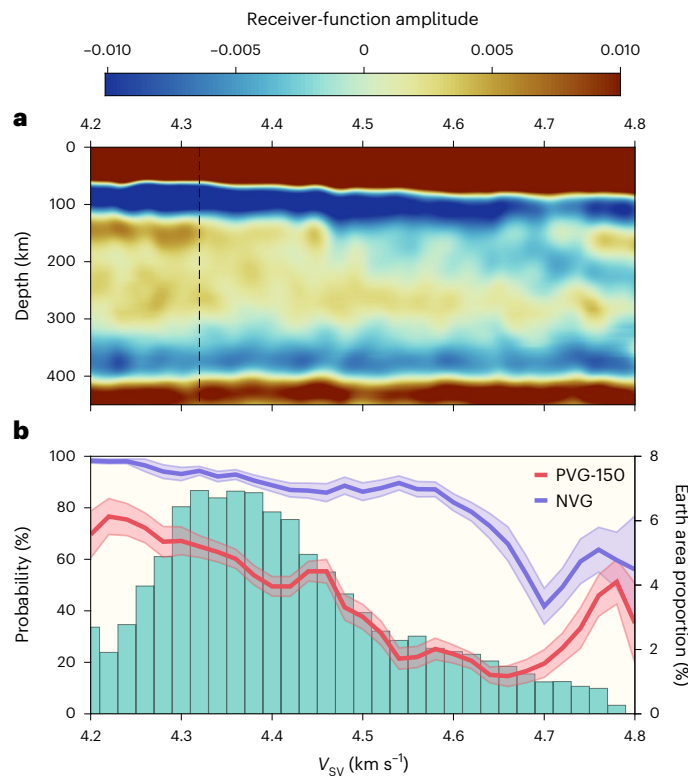


**Fig. 2 | The relationship between receiver-function phases and asthenospheric  $V_{sv}$ .** **a**, Receiver functions binned by average  $V_{sv}$  (ref. <sup>22</sup>) at depths of 110–130 km beneath the station. A clear PVG-150 phase is observed where  $V_{sv}$  is less than  $4.32 \text{ km s}^{-1}$  (dashed line). **b**, The probabilities (curves) that a PVG-150/LAB phase at the bottom/top of the LVZ is observed versus average mantle  $V_{sv}$  at depths of 110–130 km. The shaded envelopes indicate one standard deviation. Histogram shows the proportions of Earth area with a given average  $V_{sv}$  (scale at right).

a PVG are also confidently observed ( $P > 80\%$ ) at 160 stations (Fig. 1b). Another 240 stations show little evidence for this phase ( $P < 20\%$ ) (Fig. 1c), and the remaining stations cannot be confidently categorized.

We divided receiver functions into groups that represent stations with or without the PVG phase according to probability thresholds (Fig. 1e,f). Stations with the PVG phase (Fig. 1e) on average contain a higher-amplitude LAB NVG centred at depths of ~90 km. The prominent PVG phase at these stations is observed at an average depth of ~150 km. This PVG (hereafter referred to as the PVG-150) is a globally widespread observation of a clear vertically localized lower boundary to an asthenospheric LVZ and is likely to be distributed over less than 50 km in depth (Supplementary Discussion 1), complementing lower-vertical-resolution surface-wave tomography.

The stacks for the two categories have similar signals from PVGs at the Moho (depths < 50 km) and the 410 km discontinuity and from a NVG directly above the 410 km discontinuity that could represent hydrous melting due to vertical variations in water solubility<sup>23,24</sup>. Stacks for both categories also share a weak PVG at ~260 km. This deeper PVG (sometimes referred to as the ‘X discontinuity’<sup>25</sup>, but here called the PVG-260) tends to occur in broad but sporadic regions (Extended Data Fig. 2a), with a geographic distribution that differs from the PVG-150 (Fig. 1a).

## Global distribution of the low-velocity zone

Most stations with the PVG-150 lie in regions with relatively low upper-mantle shear velocities (Fig. 1a,d). To examine this relationship, we binned all the receiver functions by the average vertically polarized

shear velocities ( $V_{sv}$ ) at depths of 110–130 km (ref. <sup>22</sup>) beneath their stations (Fig. 2a). Sp receiver functions are most sensitive to  $V_{sv}$  variations, and the 110–130 km depth range represents the centre of the LVZ (Fig. 1b,e). In the velocity-binned stacks (Fig. 2a), regions with  $V_{sv}$  below  $4.32 \text{ km s}^{-1}$  contain a strong NVG at the LAB and a prominent PVG-150 marking the base of the LVZ. For  $V_{sv}$  between  $4.32$  and  $4.46 \text{ km s}^{-1}$ , a strong LAB phase is observed, but a localized PVG phase is lacking. For  $V_{sv}$  higher than  $4.46 \text{ km s}^{-1}$ , a relatively strong NVG is observed beneath the Moho, which could represent a mid-lithospheric discontinuity in the cratonic mantle<sup>9</sup>, and at depths of 120–220 km, weak NVGs are present on average. These relationships do not depend on the reference velocity model used for binning<sup>2,21</sup> (Extended Data Fig. 3), although the  $V_{sv}$  ranges for the three categories vary slightly.

Tests demonstrate that the PVG-150 phase is not an artificial side lobe of the phase from the stronger NVG at the top of the LVZ (the LAB), and that the LAB is not a side lobe of the Moho phase (Supplementary Discussion 1). The LVZ, when present, is ~65 km thick (Extended Data Fig. 4), and the average PVG-150 amplitude is matched by a velocity increase of ~4% (Extended Data Fig. 5b and Supplementary Discussion 1). In contrast to the PVG-150, the PVG-260 is, on average, present over almost the entire range of mantle velocities (Extended Data Fig. 2).

We also tested the relationship between the PVG-150 and  $V_{sv}$  separately for oceanic stations, for continental stations and with stations close to subducting lithospheric slabs removed. Overall, these cases show similar PVG-150 patterns with  $V_{sv}$ , although stations in oceanic regions tend to have higher-amplitude PVG-150 phases and higher probabilities of containing them, in particular where  $V_{sv}$  is lowest (Extended Data Fig. 3). The overall similarity indicates that the processes that produce the PVG-150 operate in low- $V_{sv}$  regions of both oceanic and continental mantle. The distribution of the PVG-150 (Fig. 1a) is broader than that of hotspots (Extended Data Fig. 2a), indicating that the PVG-150 is not restricted to plume-perturbed mantle. By extrapolating the observed PVG-150 probabilities to other regions with comparable mantle velocities (Fig. 2b and Methods), we estimated that ~44% of Earth’s area could have a LVZ with a clear PVG-150 at its base. This value might be an underestimate because most stations in this study are continental, while oceanic stations typically have higher PVG-150 probabilities (Extended Data Fig. 3m), and oceans occupy more area.

## Partial melt in the LVZ

To determine the origins of the LVZ, we first examined radial anisotropy in the solid mantle as its potential source (Supplementary Discussion 2). While radial anisotropy in either S-wave or P-wave velocities can produce phases with the same polarity as the PVG-150 (ref. <sup>26</sup>), predicted PVG phase amplitudes decrease strongly with increasing ray parameter (Extended Data Fig. 6c,d), which is not seen in the observed PVG-150 (Extended Data Fig. 6a). In addition, if typical S-wave and P-wave radial anisotropies<sup>27</sup> are combined, a notable PVG phase is not produced (Extended Data Fig. 6e). Overall, these results indicate that the PVG-150 does not originate from radial anisotropy produced by solid-state deformation and that a mechanism that leads to an isotropic velocity increase (Extended Data Fig. 6b) is sufficient.

Turning to the effects of water in the mantle, the dehydration of the residual mantle beneath mid-ocean ridges has long been thought to create a discontinuity in water content and viscosity<sup>28</sup> that could result in a NVG at the top of the LVZ. However, the solubility and partitioning of water in mantle minerals<sup>29,30</sup> indicate that the effect of water on the lower boundary of the LVZ is more gradual and would not produce the type of vertically localized velocity gradient needed to produce the observed PVG-150. Moreover, the effects of water on seismic dissipation versus grain growth may nearly cancel, resulting in negligible impact on asthenospheric seismic velocities<sup>7</sup>. Water in the asthenosphere could possibly produce the NVG phase through elastically accommodated grain boundary sliding<sup>13</sup>, but this mechanism cannot also explain the PVG-150.

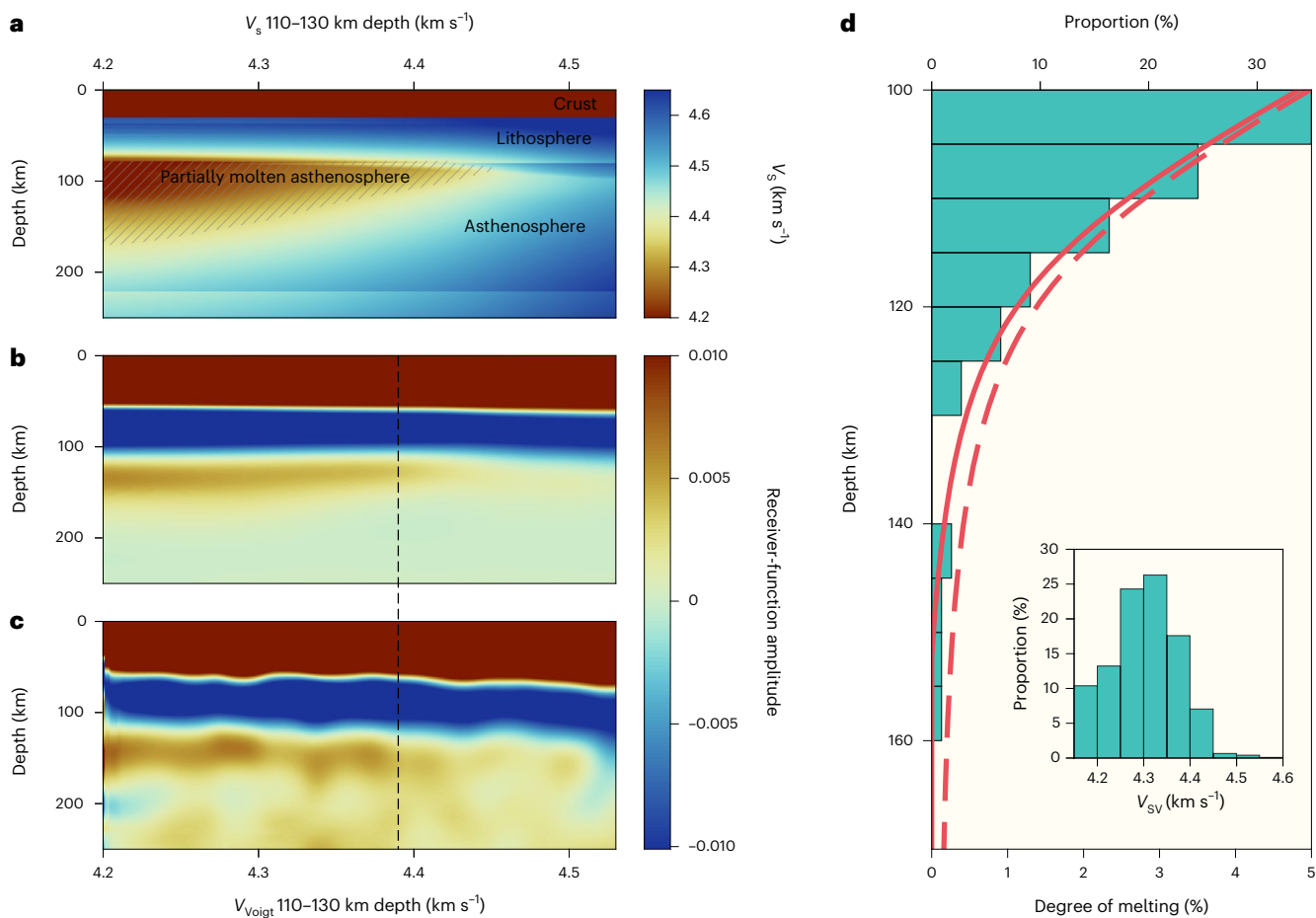


**Fig. 3 | Modelling the PVG-150 with partial melt.** **a**, Predicted seismic velocities for varying mantle conditions (Methods) binned by average isotropic  $V_s$  (110–130 km). Shading indicates average melt fraction >0.2%. **b**, Binned synthetic receiver functions predicted for velocities in **a**. **c**, Observed receiver functions binned by  $V_{\text{Voigt}}$  (110–130 km) (ref. <sup>22</sup>). Dashed line in **b** and **c** is  $V_s$ -equivalent

of dashed line in Fig. 2a. **d**, Histogram of global primary magma equilibration depths (Fig. 1a). Degree of melting<sup>37</sup> predicted for 1,450 °C mantle potential temperature and 100 ppm by weight (ppmw) water (solid line) and with additional 60 ppmw  $\text{CO}_2$  (dashed line). Inset:  $V_{\text{SV}}$  (110–130 km) for post-Pliocene basalts (all dots in Fig. 1a).

We also tested whether partial melt in the LVZ can explain the PVG-150 and whether melt is needed in addition to temperature and pressure effects. To represent the range of mantle conditions where the PVG-150 phases are observed, we calculated upper-mantle velocity models (Fig. 3a) that sample variations in mantle temperature, mineral composition and water content<sup>31</sup> and accounted for the presence of partial melt when mantle solidus temperatures were exceeded (Methods). Partial melt effects on seismic velocity were estimated on the basis of the Very Broadband Rheology calculator<sup>32</sup>, considering both the direct effect of melt on elasticity through poroelasticity<sup>33</sup> and the anelasticity effect due to variations of melt fraction<sup>34</sup>. Synthetic receiver functions were predicted for these velocity models (Methods) and were binned on the basis of their average  $V_s$  at depths of 110–130 km (Fig. 3b).

The predicted receiver functions (Fig. 3b) match several key characteristics of the observed receiver functions, with the latter now binned by  $V_{\text{Voigt}} = \sqrt{(2V_{\text{SV}}^2 + V_{\text{SH}}^2)/3}$  to represent isotropic  $V_s$  (Fig. 3c), where  $V_{\text{SH}}$  is the horizontally polarized shear velocity. At high  $V_s$ , due to temperature and pressure variations with depth and the water content difference across the LAB, a NVG receiver-function phase marking the top of the asthenosphere is generated, but the base of the LVZ is too gradual to produce a distinct phase, which is also what is observed in the global dataset. However, at higher temperatures where the asthenospheric mantle starts to melt,  $V_s$  drops and a clear PVG phase is predicted at depths and over a  $V_s$  range that match the observed PVG-150,

but only if the poroelastic effects of melt<sup>33</sup> are included (Extended Data Fig. 7, Methods and Supplementary Method 2). Minor discrepancies between the predicted and observed PVG-150 phases (Fig. 3b,c) could be accounted for by varying the reference model used to bin the data or modifying model parameters such as crustal and lithospheric thicknesses (Supplementary Discussion 3). The overall good fit between these models and the observed PVG-150 distribution favours partial melting as the origin of the LVZ. Because stations above subducting slabs could sample mantle fluxed with slab-derived fluids and experience different melting conditions, we also compared the predicted receiver functions with the observations where stations close to slabs are excluded (Extended Data Fig. 3j). Removing these stations has little effect on the observed stack overall, and the agreement between predicted and observed stacks remains. In addition, when receiver functions were binned by  $V_p/V_s$  ( $V_p/V_{\text{Voigt}}$ ) (Extended Data Fig. 3l), PVG-150 phases were associated with high  $V_p/V_s$  in the LVZ, consistent with the presence of partial melt<sup>35</sup>. Given the broadly similar distributions of the PVG-150 with  $V_s$  in the separate stacks for oceans and continents (Extended Data Fig. 3c versus 3d and Extended Data Fig. 3g versus 3h), the inferred melting occurs in high-temperature regions of both oceanic and continental asthenosphere.

To further investigate whether partial melting in the LVZ can explain the PVG-150, we analysed basalt samples erupted globally since the Pliocene (Fig. 1a). The basalts, which reflect the presence of partial melt, are concentrated where mantle velocities are 4.25–4.4 km s<sup>-1</sup> in

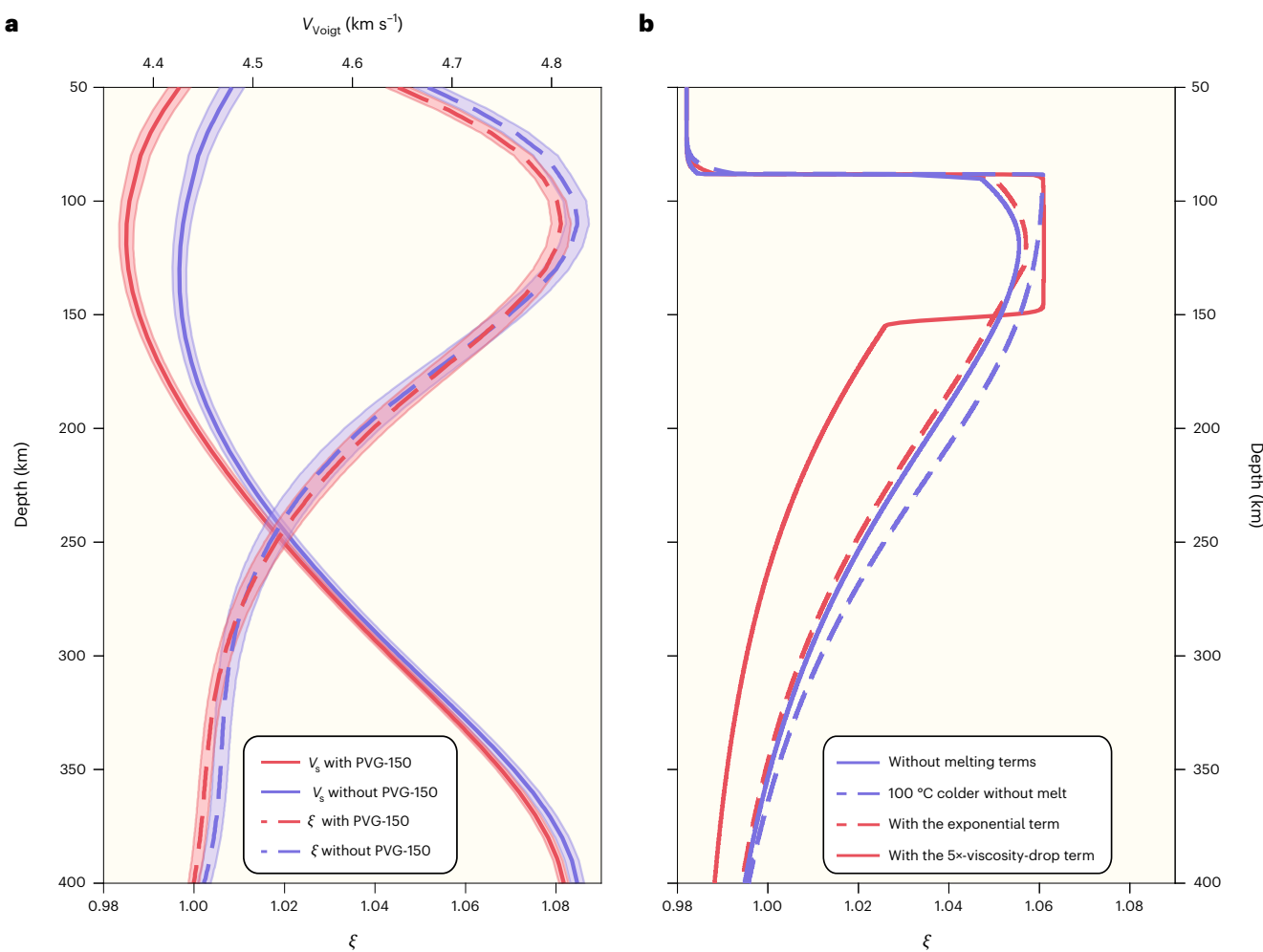


**Fig. 4 | The PVG-150, anisotropy, melt and viscosity.** **a**, Average  $V_{\text{Voigt}}$  (solid lines) and  $\xi$  (ref. <sup>22</sup>) (dashed lines) for stations with and without the PVG-150. Transparent areas indicate one standard deviation. **b**, Predicted radial anisotropy  $\xi$  (ref. <sup>12</sup>) for horizontal Couette flow (3  $\text{cm yr}^{-1}$  surface velocity and 45 Myr duration). Blue solid/dashed line: no melt effects on viscosity for

1,450 °C/1,350 °C mantle potential temperature. For 1,450 °C, melt in the LVZ affects viscosity through a moderate exponential term<sup>34</sup> (red dashed line) and via an additional factor-of-five viscosity increase below the PVG-150 (red solid line). The  $\xi$  variations from strong melt effects on viscosity (latter case) are not observed for mantle with the PVG-150 (a).

the 110–130 km depth range<sup>22</sup> (Fig. 3d, inset), and at these conditions PVG-150 phase probabilities are high (Fig. 2b). We calculated the primary magma equilibration temperatures and depths for the samples<sup>36</sup> (Supplementary Method 3), which directly reflect mantle properties where the partial melt resided before erupting, and found that the equilibration depths are consistent with the onset of melting at the depth of the PVG-150. For samples that are not strongly affected by the lithosphere, the distribution of equilibration depths follows the predicted degree of hydrous melting<sup>37</sup> that starts at ~150 km depth (Fig. 3d). This agreement is expected since depths with higher degrees of melting are more likely to be represented in the samples. If mantle CO<sub>2</sub> is also considered<sup>38</sup>, a small amount of partial melt would also exist at depths greater than 200 km and could explain the very deeply equilibrated samples (Fig. 3d) as well as the sporadically observed PVG-260, which could represent the onset of carbon-assisted melting.

### Implications for asthenospheric viscosity

To evaluate the influence of the partial melt inferred above the PVG-150 on viscosity, we determined whether regions with the PVG-150 have distinct distributions of radial anisotropy since seismic anisotropy reflects mantle deformation history<sup>12</sup>. The S-wave radial anisotropy is characterized by  $\xi = (V_{\text{Sh}}/V_{\text{Sv}})^2$ . To avoid small-scale variations that cannot be resolved in global models of radial anisotropy, we identified

the non-cratonic stations whose neighbouring stations share a similar probability for the PVG-150 phase (Extended Data Fig. 1). For these stations, average  $V_s$  ( $V_{\text{Voigt}}$ ) and  $\xi$  profiles from global models were calculated for stations with the PVG-150 phase (and presumably with partial melt in the overlying LVZ) or without. Profiles from multiple published models<sup>2,21,22,39–42</sup> based on different methodologies and datasets were compared. While regions with the PVG-150 have a reduced  $V_s$  above 200 km depth for all tested models,  $\xi$  profiles for the two groups are not significantly different (Fig. 4a and Extended Data Fig. 8a,b). Similar results are found in  $V_s$  and  $\xi$  profiles when continental and oceanic stations are examined separately (Extended Data Fig. 8e); stations with the PVG-150 have lower  $V_s$  than those without, but the differences in  $\xi$  (including slightly higher  $\xi$  values for oceanic stations without the PVG-150) are not significant. Overall, the average profiles for oceanic stations indicate lower seismic velocities and higher  $\xi$  relative to continents, but  $\xi$  is not systematically higher in the specific locations that contain the PVG-150 (and the partial melt that its presence implies), relative to locations without the PVG-150 (Extended Data Fig. 8e).

To probe the meaning of the lack of correlation between the PVG-150 and  $\xi$ , the potential impacts of partial melt within the LVZ on viscosity and the development of radial anisotropy were tested with one-dimensional (1D) and 3D mantle flow models. In the 1D models, distributions of radial anisotropy with depth were predicted for endmember cases of

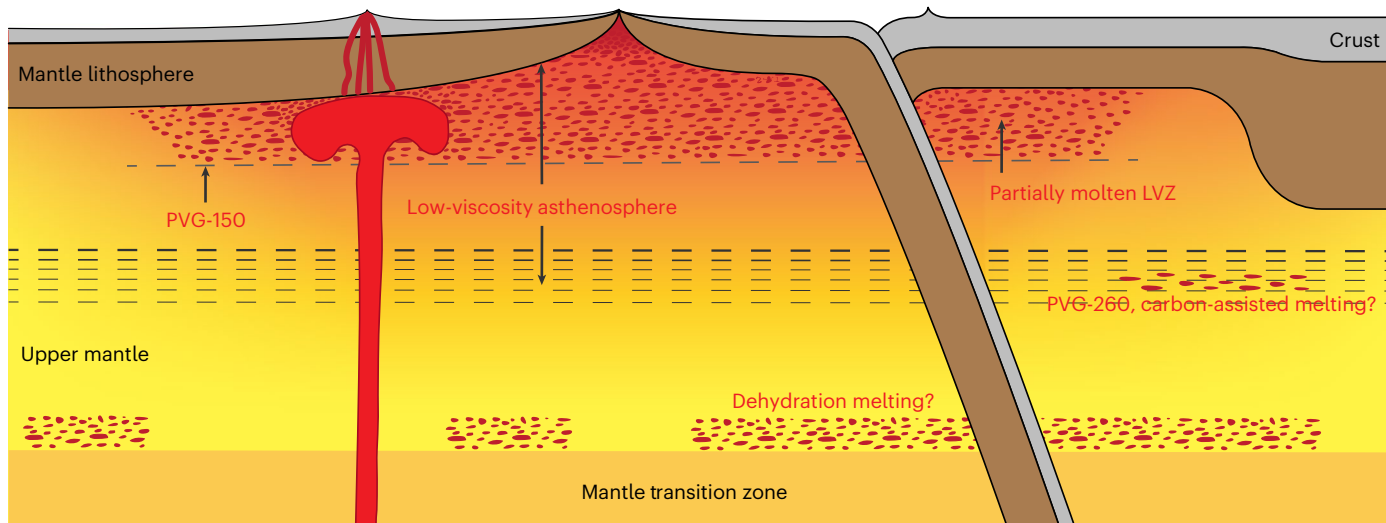


**Fig. 5 | Interpretation of the observed PVG-150 and PVG-260 mantle velocity gradients.** The PVG-150 (shallow dashed horizontal line) represents the base of a melt-rich LVZ within the asthenosphere that has little impact on viscosity. The overall low viscosity of the asthenosphere, including its gradual lower boundary

(shown by deeper dashed horizontal lines) is controlled primarily by temperature and pressure variations. The sporadically observed PVG-260 may represent the onset of carbon-assisted mantle melting. The NVG above the mantle transition zone may indicate dehydration melting due to solubility differences<sup>23,24</sup>.

asthenospheric flow: flow driven by the motion of the overriding plate (Couette flow) (Fig. 4b and Extended Data Fig. 9a) or by horizontal pressure gradients (Poiseuille flow) (Extended Data Fig. 9b). Radial anisotropy was predicted assuming three different scenarios (details in Methods): (1) partial melt has no effect on viscosity; (2) melt increases strain rate by less than 35% through an exponential term;<sup>34</sup> (3) a factor-of-five strain-rate decrease below 150 km depth that represents a sharp viscosity increase is added to the second scenario. To include the possibility that the mantle without the PVG-150 has a lower overall temperature, we also modelled radial anisotropy for a mantle potential temperature that is 100 °C colder (Fig. 4b). In contrast to the 1D modelling, where partial melt flows with its host mantle, in the 3D global mantle flow models we predicted radial anisotropy assuming the low-viscosity partially molten layers are stationary, as in ref.<sup>43</sup>. To characterize the potential effects of melt weakening, a factor-of-ten viscosity decrease was introduced at depths of 100–150 km in localized bands parallel or perpendicular to oceanic plate motion (Extended Data Fig. 10).

Both the 1D (Fig. 4b and Extended Data Fig. 9) and 3D (Extended Data Fig. 10) models of mantle flow indicate that when asthenospheric viscosity is decreased within a narrow depth range, strain is locally enhanced within the layer, leading to differences in the depth distribution of anisotropy. For example, the 1D models with the sharp viscosity drop in the layer above the PVG-150 show lower radial anisotropy in the layer below the PVG-150, even when radial-anisotropy profiles are smoothed to represent the effects of broad surface-wave sensitivity kernels during tomography (Fig. 4b and Extended Data Fig. 9). Because differences in radial anisotropy between regions with and without PVG-150 observations are not evident (Fig. 4a and Extended Data Fig. 8b), we conclude that while partial melt fraction is higher in the LVZ above the PVG-150, it does not appear to have a substantial impact on viscosity.

## Implications for partial melt in the asthenosphere

The PVG-150 mantle boundary—documented in this study to be common in high-temperature regions of the mantle on a global basis—is best explained as the base of a layer within the asthenosphere in which the presence of partial melt significantly reduces seismic velocities (Fig. 5). However, the lack of variations in seismic anisotropy and deformation that are spatially correlated with the PVG-150 indicates that the effects of variations in melt fraction on mantle viscosity are minimal. Our results thus imply that although the presence and distribution

of partial melt vary substantially within the asthenosphere, the low viscosity that defines the asthenosphere is controlled primarily by gradual temperature and pressure variations<sup>6,34</sup> (Fig. 5).

## Online content

Any methods, additional references, Nature Portfolio reporting summaries, source data, extended data, supplementary information, acknowledgements, peer review information; details of author contributions and competing interests; and statements of data and code availability are available at <https://doi.org/10.1038/s41561-022-01116-9>.

## References

- Höink, T., Lenardic, A. & Richards, M. Depth-dependent viscosity and mantle stress amplification: implications for the role of the asthenosphere in maintaining plate tectonics. *Geophys. J. Int.* **191**, 30–41 (2012).
- Priestley, K. & McKenzie, D. The relationship between shear wave velocity, temperature, attenuation and viscosity in the shallow part of the mantle. *Earth Planet. Sci. Lett.* **381**, 78–91 (2013).
- Gung, Y., Panning, M. & Romanowicz, B. Global anisotropy and the thickness of continents. *Nature* **422**, 707–711 (2003).
- Burgos, G. et al. Oceanic lithosphere–asthenosphere boundary from surface wave dispersion data. *J. Geophys. Res. Solid Earth* **119**, 1079–1093 (2014).
- Beghein, C., Yuan, K., Schmerr, N. & Xing, Z. Changes in seismic anisotropy shed light on the nature of the Gutenberg discontinuity. *Science* **343**, 1237–1240 (2014).
- Stixrude, L. & Lithgow-Bertelloni, C. Mineralogy and elasticity of the oceanic upper mantle: origin of the low-velocity zone. *J. Geophys. Res. Solid Earth* **110**, B03204 (2005).
- Abers, G. A. et al. Reconciling mantle attenuation–temperature relationships from seismology, petrology, and laboratory measurements. *Geochem. Geophys. Geosyst.* **15**, 3521–3542 (2014).
- Debayle, E., Bodin, T., Durand, S. & Ricard, Y. Seismic evidence for partial melt below tectonic plates. *Nature* **586**, 555–559 (2020).
- Fischer, K. M. et al. A comparison of oceanic and continental mantle lithosphere. *Phys. Earth Planet. Inter.* **309**, 106600 (2020).
- Holtzman, B. K. Questions on the existence, persistence, and mechanical effects of a very small melt fraction in the asthenosphere. *Geochem. Geophys. Geosyst.* **17**, 470–484 (2016).

11. Selway, K. & O'Donnell, J. P. A small, unextractable melt fraction as the cause for the low velocity zone. *Earth Planet. Sci. Lett.* **517**, 117–124 (2019).
12. Hansen, L. N., Qi, C. & Warren, J. M. Olivine anisotropy suggests Gutenberg discontinuity is not the base of the lithosphere. *Proc. Natl Acad. Sci. USA* **113**, 10503–10506 (2016).
13. Karato, S.-i On the origin of the asthenosphere. *Earth Planet. Sci. Lett.* **321**, 95–103 (2012).
14. Ma, Z. et al. Shear attenuation and anelastic mechanisms in the central Pacific upper mantle. *Earth Planet. Sci. Lett.* **536**, 116148 (2020).
15. Kind, R., Yuan, X. & Kumar, P. Seismic receiver functions and the lithosphere–asthenosphere boundary. *Tectonophysics* **536**, 25–43 (2012).
16. Liu, T. & Shearer, P. M. Complicated lithospheric structure beneath the contiguous US revealed by teleseismic S reflections. *J. Geophys. Res. Solid Earth* **126**, e2020JB021624 (2020).
17. Rychert, C. A., Laske, G., Harmon, N. & Shearer, P. M. Seismic imaging of melt in a displaced Hawaiian plume. *Nat. Geosci.* **6**, 657–660 (2013).
18. Wu, Z. et al. Lateral Structural Variation of the Lithosphere-Asthenosphere System in the Northeastern to Eastern Iranian Plateau and Its Tectonic Implications. *J. Geophys. Res. Solid Earth* **126**, e2020JB020256 (2021).
19. Hua, J., Fischer, K. M., Wu, M. & Blom, N. A. New approaches to multifrequency Sp stacking tested in the Anatolian region. *J. Geophys. Res. Solid Earth* **125**, e2020JB020313 (2020).
20. Miller, M. S., O'Driscoll, L. J., Butcher, A. J. & Thomas, C. Imaging Canary Island hotspot material beneath the lithosphere of Morocco and southern Spain. *Earth Planet. Sci. Lett.* **431**, 186–194 (2015).
21. French, S. W. & Romanowicz, B. Broad plumes rooted at the base of the Earth's mantle beneath major hotspots. *Nature* **525**, 95–99 (2015).
22. Lei, W. et al. Global adjoint tomography—model GLAD-M25. *Geophys. J. Int.* **223**, 1–21 (2020).
23. Karato, S.-i Water distribution across the mantle transition zone and its implications for global material circulation. *Earth Planet. Sci. Lett.* **301**, 413–423 (2011).
24. Freitas, D. & Manthilake, G. Electrical conductivity of hydrous silicate melts: implications for the bottom-up hydration of Earth's upper mantle. *Earth Planet. Sci. Lett.* **523**, 115712 (2019).
25. Pugh, S., Jenkins, J., Boyce, A. & Cottaar, S. Global receiver function observations of the X-discontinuity reveal recycled basalt beneath hotspots. *Earth Planet. Sci. Lett.* **561**, 116813 (2021).
26. Kawakatsu, H. Unexpected consequences of transverse isotropy. *Bull. Seismol. Soc. Am.* **111**, 129–138 (2021).
27. Dziewonski, A. M. & Anderson, D. L. Preliminary reference Earth model. *Phys. Earth Planet. Inter.* **25**, 297–356 (1981).
28. Hirth, G. & Kohlstedt, D. L. Water in the oceanic upper mantle: implications for rheology, melt extraction and the evolution of the lithosphere. *Earth Planet. Sci. Lett.* **144**, 93–108 (1996).
29. Mierdel, K., Keppler, H., Smyth, J. R. & Langenhorst, F. Water solubility in aluminous orthopyroxene and the origin of Earth's asthenosphere. *Science* **315**, 364–368 (2007).
30. Hirschmann, M. M. Water, melting, and the deep Earth H<sub>2</sub>O cycle. *Annu. Rev. Earth Planet. Sci.* **34**, 629–653 (2006).
31. Jackson, I. & Faul, U. H. Grainsize-sensitive viscoelastic relaxation in olivine: towards a robust laboratory-based model for seismological application. *Phys. Earth Planet. Inter.* **183**, 151–163 (2010).
32. Havlin, C., Holtzman, B. K. & Hopper, E. Inference of thermodynamic state in the asthenosphere from anelastic properties, with applications to North American upper mantle. *Phys. Earth Planet. Inter.* **314**, 106639 (2021).
33. Takei, Y. Constitutive mechanical relations of solid–liquid composites in terms of grain-boundary contiguity. *J. Geophys. Res. Solid Earth* **103**, 18183–18203 (1998).
34. Hirth, G. & Kohlstedt, D. L. in *Inside the Subduction Factory* (ed. Eiler, J.) 83–106 (American Geophysical Union, 2003).
35. Hammond, W. C. & Humphreys, E. D. Upper mantle seismic wave velocity: effects of realistic partial melt geometries. *J. Geophys. Res. Solid Earth* **105**, 10975–10986 (2000).
36. Lee, C.-T. A., Luffi, P., Plank, T., Dalton, H. & Leeman, W. P. Constraints on the depths and temperatures of basaltic magma generation on Earth and other terrestrial planets using new thermobarometers for mafic magmas. *Earth Planet. Sci. Lett.* **279**, 20–33 (2009).
37. Hirschmann, M. M. Partial melt in the oceanic low velocity zone. *Phys. Earth Planet. Inter.* **179**, 60–71 (2010).
38. Dasgupta, R. et al. Carbon-dioxide-rich silicate melt in the Earth's upper mantle. *Nature* **493**, 211–215 (2013).
39. Chang, S. J., Ferreira, A. M., Ritsema, J., van Heijst, H. J. & Woodhouse, J. H. Joint inversion for global isotropic and radially anisotropic mantle structure including crustal thickness perturbations. *J. Geophys. Res. Solid Earth* **120**, 4278–4300 (2015).
40. Ho, T., Priestley, K. & Debayle, E. A global horizontal shear velocity model of the upper mantle from multimode Love wave measurements. *Geophys. J. Int.* **207**, 542–561 (2016).
41. Moulik, P. & Ekström, G. An anisotropic shear velocity model of the Earth's mantle using normal modes, body waves, surface waves and long-period waveforms. *Geophys. J. Int.* **199**, 1713–1738 (2014).
42. Porritt, R. W., Becker, T. W., Boschi, L. & Auer, L. Multiscale, radially anisotropic shear wave imaging of the mantle underneath the contiguous United States through joint inversion of USArray and global data sets. *Geophys. J. Int.* **226**, 1730–1746 (2021).
43. Becker, T. W. Superweak asthenosphere in light of upper mantle seismic anisotropy. *Geochem. Geophys. Geosyst.* **18**, 1986–2003 (2017).

**Publisher's note** Springer Nature remains neutral with regard to jurisdictional claims in published maps and institutional affiliations.

Springer Nature or its licensor (e.g. a society or other partner) holds exclusive rights to this article under a publishing agreement with the author(s) or other rightsholder(s); author self-archiving of the accepted manuscript version of this article is solely governed by the terms of such publishing agreement and applicable law.

© The Author(s), under exclusive licence to Springer Nature Limited 2023

## Methods

### Sp receiver functions and the velocity gradients they imply

Seismograms from 716 stations were downloaded from the IRIS Data Management Center, and receiver functions were calculated using the approach in ref. <sup>19</sup>. For earthquakes with a moment magnitude greater than 5.8 (1980 onwards), we requested waveforms around S arrivals with epicentral distances between 55° and 85°, and waveforms around P arrivals with distances between 35° and 80°; P arrivals were used only for determining near-surface velocities and H-k stacking<sup>45</sup> during data processing, while S arrivals were also used to obtain the Sp receiver functions for analysis. The seismograms were transformed to P and SV components on the basis of a free-surface transform with free-surface  $V_p$  and  $V_s$  measured for each station<sup>19</sup>.

To obtain accurate Sp receiver-function stacks for each station, we first calculated time-domain deconvolved Sp receiver functions<sup>44</sup> for each event after filtering the waveforms to 10–100 s periods to better capture relatively gradual velocity changes (Extended Data Fig. 5). We then used a combination of H-k stacking<sup>45</sup> and the global velocity model GLAD-M25<sup>22</sup> to migrate the time-domain receiver functions to depth. The migrated receiver functions underwent quality control, and the remaining 184,340 receiver functions were stacked by station to obtain a representative average receiver function and the covariance matrix between amplitudes at different depths through bootstrapping. Detailed information regarding migration and the processing of the receiver functions is provided in Supplementary Method 1.

The probability ( $P$ ) that a PVG or NVG phase is present was estimated from the stacked Sp receiver functions and their covariance using a Monte Carlo approach. For each station, the stacked receiver functions were randomly perturbed 3,000 times on the basis of their bootstrap-estimated covariance, and the phases were picked from each perturbed receiver function using an automated algorithm (Extended Data Fig. 1a). The probability that a phase exists was evaluated as the ratio between the number of times that a phase was successfully picked from the perturbed receiver function and 3,000. When picking the PVG-150 phase in the 100–200 km depth range, criteria were that the phase had to exceed amplitudes of 0.003 over at least 15 km in depth, have a width (defined as three times the depth range corresponding to the standard deviation of the phase as in ref. <sup>46</sup>) of more than 10 km and reach an amplitude of at least 0.006 (Extended Data Fig. 1a). Probabilities for the PVG-260 phases (Extended Data Fig. 2) were evaluated in the same manner but in the depth range between 230 and 350 km (ref. <sup>25</sup>). Probabilities for NVG phases were determined similarly but from depths of 40–140 km using negative receiver-function amplitudes and with threshold amplitudes of 0.004 and a minimum required maximum amplitude of 0.008. For all phases, probabilities were estimated only for the 608 stations whose receiver-function stacks contained more than 40 individual Sp receiver functions.

The distributions of picked PVG-150 and NVG depths and amplitudes for non-cratonic stations (bins where average  $V_{sv} < 4.46 \text{ km s}^{-1}$  at 110–130 km depths) are shown in Extended Data Fig. 4, and the spatial distributions of PVG-150 depths and amplitudes are shown in Extended Data Fig. 1. For the non-cratonic stations, we found the median values for the depths of the LAB and PVG-150 are 88 km (with an interquartile range of 12 km) and 152 km (with an interquartile range of 29 km). Using stations with observations of both phases, while satisfying the  $V_{sv}$  requirement, the median thickness of the LVZ is estimated to be 65 km (with an interquartile range of 21 km) (Extended Data Fig. 4).

### Receiver-function binning as a function of upper-mantle properties

To calculate binned receiver functions as a function of mantle properties (average  $V_{sv}$  (Fig. 2a and Extended Data Fig. 3),  $V_p/V_s$  (Extended Data Fig. 3) and  $V_{voigt}$  (Fig. 3c and Extended Data Fig. 3) at 110–130 km depths) and of ray parameter (Extended Data Fig. 6), a weighted averaging method was used. The binned receiver-function amplitude (RF)

for a property  $X$  at a depth  $h$  was expressed as a weighted average of all receiver functions:

$$RF(X, h) = \frac{\sum_i W_1(X, X_i) r_f_i(h)}{\sum_i W_1(X, X_i)}, \quad (1)$$

where  $W_1$  is the weighting function,  $r_f$  is the  $i^{\text{th}}$  receiver function and  $X_i$  is the corresponding property for the  $i^{\text{th}}$  individual receiver function. The weighting function is designed to be a Gaussian

$$W_1(X, X_i) = \exp \left[ -\frac{(X - X_i)^2}{2\sigma_X^2} \right], \quad (2)$$

where  $\sigma_X$  regulates the averaging width, and the weight is set to zero if the difference between  $X$  and  $X_i$  is higher than  $3\sigma_X$ . When binning by  $V_{sv}$  and  $V_{voigt}$ ,  $\sigma_X$  is set to  $0.01 \text{ km s}^{-1}$ ; for  $V_p/V_s$ ,  $\sigma_X$  is set to 0.002; and for ray parameter,  $\sigma_X$  is  $0.001 \text{ s km}^{-1}$ . For the binning, receiver functions from all 716 stations were used.

### PVG-150 and LAB probabilities and the global extent of the PVG-150

We calculated the probability of the occurrence of the PVG-150 or NVG (LAB) phases as a function of  $V_{sv}$  (Fig. 2b) and  $V_p/V_s$  (Extended Data Fig. 3l) on the basis of the 608 stations where phase probabilities were estimated. For the case of  $V_{sv}$ , at each  $V_{sv}$  value, we identified stations whose average  $V_{sv}$  at 110–130 km depth is within  $0.025 \text{ km s}^{-1}$  of the given value and calculated the mean and standard deviation of the phase probabilities at these stations (Fig. 2b and Extended Data Fig. 3m). For the case of  $V_p/V_s$  (Extended Data Fig. 3l), the same approach was used, but the range around each  $V_p/V_s$  value was 0.005. These mean values are taken to represent PVG-150 or LAB probabilities as a function of  $V_{sv}$  or  $V_p/V_s$ .

We estimated the global extent of the LVZ with a clear lower PVG-150 boundary by assuming the PVG-150 probability with  $V_{sv}$  estimated from the 608 stations can be applied to other regions with comparable mantle velocities (Fig. 2b). For regions with  $V_{sv} < 4.35 \text{ km s}^{-1}$ , the probability is higher than 60%, indicating a prevalent PVG-150 phase. In contrast, for cratonic regions with  $V_{sv}$  from 4.5 to 4.7  $\text{km s}^{-1}$ , the probability is minimal, and although the probability increases again at very high  $V_{sv}$ , these PVGs probably lie within the cratonic lithosphere. The area of Earth that has an asthenospheric LVZ with a clear PVG-150 at its base was estimated by integrating the product of the probability and the proportion of Earth with a given velocity for  $V_{sv}$  from  $4.2 \text{ km s}^{-1}$  to  $4.46 \text{ km s}^{-1}$  (non-cratonic regions) (Fig. 2a). The resulting area is 44%.

### Average depth profiles of mantle properties

Average mantle property profiles with depth ( $V_{voigt}$ , radial anisotropy ( $\xi$ ), attenuation and radial mantle flow velocity) were obtained for non-cratonic regions with or without the PVG-150 phase (Fig. 4a and Extended Data Fig. 8). In some regions, neighbouring stations show highly variable PVG-150 probabilities (Fig. 1a), and because mantle properties from global tomographic models are not able to resolve structure at these scales, those stations were downweighted. To design the latter weighting function, we first obtained a smoothed global map for the probability of the PVG-150 where the probability at a given location is the weighted average of PVG-150 probability among stations within 480 km of that location. The weight for each station is given by

$$W_2(D) = \exp \left( -\frac{D^2}{2\sigma_D^2} \right), \quad (3)$$

where  $D$  is the distance from the map location to that station, and the critical distance  $\sigma_D$  is set to 200 km (Extended Data Fig. 1d). This weighting function was also applied to calculate the standard deviation

of the PVG-150 probability among neighbouring stations to obtain a map characterizing local probability variations (Extended Data Fig. 1e).

The weighting function to obtain the representative mantle property profiles was defined as

$$W_3(P) = \exp\left[-\frac{(P - P_{\text{map}})^2}{2\sigma_p^2}\right] \exp\left(-\frac{P_{\text{std}}^2}{2\sigma_p^2}\right), \quad (4)$$

where  $P$  represents the PVG-150 phase probability at a station,  $P_{\text{map}}$  is the probability at the station location from the smoothed probability map,  $P_{\text{std}}$  is the value at the station location from the standard deviation map and  $\sigma_p$  is set to 0.2. With this formulation, stations whose probabilities contradict surrounding stations and stations at locations with a larger range of probabilities, which indicate small-scale structures, are penalized. As shown in Extended Data Fig. 1f, all stations where  $W_3$  is higher than 0.4 are either isolated or close to stations with similar probabilities of the PVG-150 phase. Hence, with this weighting function, the averaged representative mantle profiles from global tomographic models for regions with and without the phase (Fig. 4a and Extended Data Fig. 8) are more reliable. This method will also prioritize stations with no neighbours, but those stations are concentrated mostly in the oceans, where mantle structure is relatively homogeneous (Extended Data Fig. 1f). The weighted average was applied to 134 stations with the phase ( $P > 0.8$ ) and 75 stations without the phase ( $P < 0.2$ ), including only stations with an average  $V_s$  at 110–130 km depth below 4.46 km s<sup>-1</sup> to avoid cratons. Standard deviations for the weighted averaged mantle profiles were also estimated<sup>19</sup> (Fig. 4a and Extended Data Fig. 8). Average mantle profiles appear in Extended Data Fig. 8a for  $V_{\text{Voigt}}$ , Extended Data Fig. 8b for radial anisotropy, Extended Data Fig. 8c for attenuation and Extended Data Fig. 8d for radial mantle flow velocities.

### Comparison of mantle thermal models with partial melt with Sp receiver functions

To assess whether partial melt in the asthenosphere is required to match the observed Sp receiver functions, models of mantle properties with and without partial melt effects were converted to seismic velocities (Fig. 3a), the propagator matrix method<sup>47</sup> was used to calculate synthetic receiver functions, and the receiver functions were binned by predicted  $V_s$  in the 110–130 km depth range (Fig. 3b).

In the candidate thermal models, we assumed a 30-km-thick crust above anhydrous conductive mantle lithosphere. The prescribed lithospheric thickness varied linearly with mantle potential temperature (78 km for 1,450 °C and 98 km for 1,250 °C). This variation partially accounts for the apparent LAB deepening with  $V_s$  (Fig. 3c), although the full range of observed LAB depths is wider (Extended Data Fig. 4). In the underlying adiabatic asthenosphere, we assumed mantle potential temperatures between 1,250 and 1,450 °C and a grain size of 10 mm. This temperature range was chosen to be slightly greater than the ambient mantle temperature of 1,300–1,400 °C (ref. <sup>48</sup>), and the grain size is consistent with grain-size evolution models<sup>49,50</sup> and mantle xenoliths<sup>7</sup>. The influence of the assumed grain size is discussed in Supplementary Discussion 3. For each mantle potential temperature, 256 different cases were considered, assuming an asthenospheric mantle water content ranging from 0 to 300 ppm by weight (ppmw) with an interval of 20 ppmw and a maximum allowed melt fraction between 0 and 1.5% with an interval of 0.1%. The melt fraction was set to be the same as the degree of hydrous melting for the geotherm when the maximum allowed melt fraction was not reached; otherwise, it was set to be equal to that maximum value, assuming any additional melt was extracted. Details regarding mantle adiabats and calculations of the degree of melting are provided in Supplementary Method 2.

For each of these models, elastic seismic velocities were calculated with Perple\_X<sup>51</sup> (Supplementary Method 2) for the mantle to account for variations in mineral composition, and a  $V_s$  of 3.9 km s<sup>-1</sup> was assumed in the crust. Where partial melt was predicted in a given model, its

poroelastic effect was included using refs. <sup>33,52</sup> as implemented in the Very Broadband Rheology calculator<sup>32</sup>, and its anelastic effect was incorporated according to ref. <sup>31</sup>, assuming the high-temperature background for a seismic wave period of 15 s as the effect from the absorption peak is relatively uncertain and could be depth dependent<sup>14</sup>. The influence of water on anelasticity is from ref. <sup>7</sup>.

To evaluate whether 0–1.5% is a reasonable range for melt fraction, we also estimated the required melt fraction for the PVG-150 according to ref. <sup>53</sup>. This experimental study provides a relationship between melt fraction and  $V_s$  but does not isolate the poroelastic effect from anelasticity. Using the relationship between  $V_s$  and melt fraction in ref. <sup>53</sup>, to achieve the velocity change of ~4% estimated for the PVG-150 phase (Extended Data Fig. 5), a melt fraction of ~0.33% is required. This value falls within the range of 0–1.5% used in the velocity models described in the preceding paragraph.

Synthetic receiver functions were calculated for each of the velocity models and binned by their average  $V_s$  at depths of 110–130 km (Fig. 3b). When calculating the average  $V_s$ , we first calculated  $V_s$  at a 150 s period to better represent seismic phases used for global tomography and then transformed that value to  $V_s$  at 1 s assuming the attenuation in PREM<sup>27</sup>, which is the attenuation model assumed in GLAD-M25 (ref. <sup>22</sup>), so that the synthetics (Fig. 3b) can be directly compared with the observed stacked receiver functions (Fig. 3c) using the same  $x$  axis. However, this approach introduces apparent velocity boundaries at 80 and 220 km because of attenuation discontinuities in PREM<sup>27</sup> at those depths (Fig. 3a). The binning of the  $V_s$  profiles (Fig. 3a) and receiver functions (Fig. 3b) as a function of average  $V_s$  at 110–130 km depths was carried out with the weighted averaging approach in equation (1). The binned receiver-function patterns are discussed in more detail in Supplementary Discussion 3.

### Modelling the development of radial anisotropy with 1D models

To model flow, the upper mantle was characterized by an adiabat for a mantle potential temperature of 1,450 °C with thermodynamic parameters specified in ref. <sup>54</sup>, and mantle water content was assumed to be 100 ppmw. These mantle conditions were chosen because they allow melting to initiate at around 150 km depth<sup>55</sup> and could represent primary magma equilibration conditions of the hot basalt samples (Supplementary Method 3), although similar melting depths could also be produced for a lower-temperature mantle with higher volatile content. Since this modelling effort is intended to show the consequence of a sharp viscosity change at the melting depth, the specific selected mantle conditions are not crucial. Above an adiabatic asthenosphere, an 88-km-thick conductive lithosphere was assumed, with a crustal thickness of 30 km. Densities for crust and mantle were assumed to be 2,800 kg m<sup>-3</sup> and 3,300 kg m<sup>-3</sup>. On the basis of these mantle properties, we estimated viscous flow velocities by considering both dislocation and diffusion creep<sup>34</sup>. Details about how the flow velocities were obtained are given in Supplementary Method 4.

With the resulting flow velocities (Extended Data Fig. 9), the strain rates for dislocation creep and diffusion creep were obtained, together with the corresponding strain accumulation over time. Since dislocation creep on glide planes produces crystallographic preferred orientations that lead to seismic anisotropy, the accumulated dislocation strain was converted to radial anisotropy  $\xi$  (ref. <sup>12</sup>) (Fig. 4b and Extended Data Fig. 9). The resulting radial-anisotropy profiles illustrate that a strong reduction in mantle viscosity due to partial melt would produce a sharp reduction in radial anisotropy below the lower boundary of the LVZ. The absence of discernable differences in observed radial-anisotropy profiles with and without the PVG-150 phase (Fig. 4a) is inconsistent with this prediction, leading to the conclusion that partial melt in the LVZ does not have a strong effect on viscosity. Since radial anisotropy from the relationship in ref. <sup>12</sup> saturates at ~1.06, stronger anisotropy observed in tomographic models cannot

be predicted from this 1D modelling. Nonetheless, the results of this modelling show that there is no evidence for a viscosity boundary at the base of the LVZ.

To include the possibility of potentially lower mantle temperatures in regions without the PVG-150, we also modelled the Couette flow radial anisotropy for a colder (1,350 °C) mantle (Fig. 4b). Because the modelled 1D anisotropy essentially depends on the strain-rate distribution with depth, for Couette flow, with the same prescribed surface motion and similar relative viscosity distributions due to similar geothermal gradients, the strain-rate and radial-anisotropy distributions with depth are similar for different temperatures (Fig. 4b), although the values of stress do differ. For Poiseuille flow, with the prescribed pressure gradient, both the overall stress and the relative viscosity would be distributed with depth similarly for adiabats at different temperatures, resulting in different absolute values of the strain rate. Nonetheless, the relative strain-rate distributions would still be similar despite these temperature variations, so if different accumulation times are allowed, the shape of the radial anisotropy would also be similar for different temperatures.

### Modelling the development of radial anisotropy with 3D models

The 3D models also show that layers of low-viscosity asthenosphere, as potentially created by partial melt, should produce an observable effect on  $\xi$ . Starting with the geodynamic models from ref. <sup>43</sup>, where only azimuthal anisotropy was analysed, in this study, we extracted radial-anisotropy patterns using the same approach<sup>56,57</sup>. In some model cases<sup>43</sup>, oceanic regions contain elongated bands at 100–150 km depths in which viscosity is reduced by a factor of 10 compared with a reference viscosity model (Extended Data Fig. 10). The introduction of these low-viscosity bands substantially modifies predicted patterns of radial anisotropy, including its distribution with depth (Extended Data Fig. 10). At 100 km, near the top of the low-viscosity bands,  $\xi$  values are increased, and at 200 km, in ‘normal’ mantle below the low-viscosity bands, radial anisotropy is relatively low compared with the neighbouring mantle. These effects are similar to the reduction in radial anisotropy in the mantle below the lowest-viscosity asthenospheric layer in the 1D models. While the details depend on modelling assumptions, relative changes due to the viscosity reduction patches are robust<sup>43</sup>, and any viscosity reduction at comparable scales should be reflected in seismic anisotropy. Therefore, the 3D model results likewise argue against the PVG-150 being a distinctive viscosity boundary since regions with and without the PVG-150 have similar distributions of radial anisotropy (Fig. 4a).

The conclusion that partial melt in the LVZ above the PVG-150 does not substantially reduce viscosity is furthermore supported by comparing average attenuation profiles from global tomography models<sup>58,59</sup>. If the PVG-150 is a diffusion creep viscosity boundary, it could introduce a strong anelasticity effect<sup>10</sup>. However, the average attenuation profiles for regions with and without the PVG-150 are similar (Extended Data Fig. 8), which demonstrates that a strong  $V_s$  reduction in the presence of a small amount of partial melt due to anelasticity<sup>10</sup> (for example, Extended Data Fig. 7b) is not the cause of the PVG-150.

### Data availability

Seismograms were downloaded from the IRIS Data Management Center (<http://ds.iris.edu/ds/nodes/dmc/>). The Sp receiver functions for all stations are available as raw data on the Figshare platform (<https://doi.org/10.6084/m9.figshare.21706325>). Geochemical data were downloaded from GEOROC (<http://georoc.mpch-mainz.gwdg.de/Georoc>) and are provided as Supplementary Table 1. Velocity model GLAD-M25 (ref. <sup>22</sup>) was obtained from E. Bozdag. Velocity models SEMUCB-WM1 (ref. <sup>21</sup>) and SEMUCB-UMQ<sup>59</sup> were downloaded from the Berkeley Global Seismology Group ([http://seismo.berkeley.edu/wiki\\_br/Main\\_Page](http://seismo.berkeley.edu/wiki_br/Main_Page)). Velocity Model SAVANI-US<sup>42</sup> was from T. W. Becker’s website (<http://www-udc.ig.utexas.edu/external/becker/tdata.html>). The

attenuation model QRFSI12 (ref. <sup>58</sup>) was from C. A. Dalton’s website (<http://www.geo.brown.edu/research/Dalton/downloads.html>); QsADR17 (ref. <sup>60</sup>) was from E. Debye’s website (<http://perso.ens-lyon.fr/eric.debaye/>). Other velocity models, including CAM2016 (refs. <sup>2,40</sup>), S362ANI + M<sup>41</sup> and SGLOBE-rani<sup>39</sup> were from the IRIS archive (<https://ds.iris.edu/ds/products/emc-earthmodels/>).

### Code availability

All computer codes used for data processing, analysis and plotting are available on request.

### References

44. Ligorría, J. P. & Ammon, C. J. Iterative deconvolution and receiver-function estimation. *Bull. Seismol. Soc. Am.* **89**, 1395–1400 (1999).
45. Rychert, C. A. & Harmon, N. Stacked P-to-S and S-to-P receiver functions determination of crustal thickness,  $V_p$ , and  $V_s$ : the H-V stacking method. *Geophys. Res. Lett.* **43**, 1487–1494 (2016).
46. Hua, J., Fischer, K. M. & Savage, M. K. The lithosphere–asthenosphere boundary beneath the South Island of New Zealand. *Earth Planet. Sci. Lett.* **484**, 92–102 (2018).
47. Keith, C. M. & Crampin, S. Seismic body waves in anisotropic media: synthetic seismograms. *Geophys. J. Int.* **49**, 225–243 (1977).
48. Herzberg, C. & Gazel, E. Petrological evidence for secular cooling in mantle plumes. *Nature* **458**, 619–622 (2009).
49. Behn, M. D., Hirth, G. & Elsenbeck, J. R. II Implications of grain size evolution on the seismic structure of the oceanic upper mantle. *Earth Planet. Sci. Lett.* **282**, 178–189 (2009).
50. Turner, A. J., Katz, R. F. & Behn, M. D. Grain-size dynamics beneath mid-ocean ridges: implications for permeability and melt extraction. *Geochem. Geophys. Geosyst.* **16**, 925–946 (2015).
51. Connolly, J. The geodynamic equation of state: what and how. *Geochem. Geophys. Geosyst.* **10**, Q10014 (2009).
52. Takei, Y. Effect of pore geometry on  $V_p/V_s$ : from equilibrium geometry to crack. *J. Geophys. Res. Solid Earth* <https://doi.org/10.1029/2001JB000522> (2002).
53. Chantel, J. et al. Experimental evidence supports mantle partial melting in the asthenosphere. *Sci. Adv.* **2**, e1600246 (2016).
54. Katz, R. F., Spiegelman, M. & Langmuir, C. H. A new parameterization of hydrous mantle melting. *Geochem. Geophys. Geosyst.* <https://doi.org/10.1029/2002GC000433> (2003).
55. Hirschmann, M. M., Tenner, T., Aubaud, C. & Withers, A. C. Dehydration melting of nominally anhydrous mantle: the primacy of partitioning. *Phys. Earth Planet. Inter.* **176**, 54–68 (2009).
56. Kaminski, E., Ribe, N. M. & Browaeys, J. T. D-Rex, a program for calculation of seismic anisotropy due to crystal lattice preferred orientation in the convective upper mantle. *Geophys. J. Int.* **158**, 744–752 (2004).
57. Becker, T. W., Kustowski, B. & Ekström, G. Radial seismic anisotropy as a constraint for upper mantle rheology. *Earth Planet. Sci. Lett.* **267**, 213–227 (2008).
58. Dalton, C. A., Ekström, G. & Dziewoński, A. M. The global attenuation structure of the upper mantle. *J. Geophys. Res. Solid Earth* **113**, B09303 (2008).
59. Karaoğlu, H. & Romanowicz, B. Inferring global upper-mantle shear attenuation structure by waveform tomography using the spectral element method. *Geophys. J. Int.* **213**, 1536–1558 (2018).
60. Adenis, A., Debye, E. & Ricard, Y. Attenuation tomography of the upper mantle. *Geophys. Res. Lett.* **44**, 7715–7724 (2017).
61. Courtillot, V., Davaille, A., Besse, J. & Stock, J. Three distinct types of hotspots in the Earth’s mantle. *Earth Planet. Sci. Lett.* **205**, 295–308 (2003).
62. Richards, M. A., Hager, B. H. & Sleep, N. H. Dynamically supported geoid highs over hotspots: observation and theory. *J. Geophys. Res. Solid Earth* **93**, 7690–7708 (1988).

63. Steinberger, B. Plumes in a convecting mantle: models and observations for individual hotspots. *J. Geophys. Res. Solid Earth* **105**, 11127–11152 (2000).
64. Bird, P. An updated digital model of plate boundaries. *Geochem. Geophys. Geosyst.* **4**, 1027 (2003).
65. Laske, G., Masters, G., Ma, Z. & Pasyanos, M. Update on Crust 1.0: a 1-degree global model of Earth's crust. *Geophys. Res. Abstr.* **15**, abstr. 2658 (2013).
66. Hayes, G. P. et al. Slab2, a comprehensive subduction zone geometry model. *Science* **362**, 58–61 (2018).
67. Yamauchi, H. & Takei, Y. Polycrystal anelasticity at near-solidus temperatures. *J. Geophys. Res. Solid Earth* **121**, 7790–7820 (2016).
68. Lu, C., Grand, S. P., Lai, H. & Garnero, E. J. TX2019slab: a new P and S tomography model incorporating subducting slabs. *J. Geophys. Res. Solid Earth* **124**, 11549–11567 (2019).
69. Conrad, C. P. & Behn, M. D. Constraints on lithosphere net rotation and asthenospheric viscosity from global mantle flow models and seismic anisotropy. *Geochem. Geophys. Geosyst.* **11**, Q05W05 (2010).
70. Stixrude, L. & Lithgow-Bertelloni, C. Thermodynamics of mantle minerals—II. Phase equilibria. *Geophys. J. Int.* **184**, 1180–1213 (2011).
71. McKenzie, D. The generation and compaction of partially molten rock. *J. Petrol.* **25**, 713–765 (1984).
72. Turcotte, D. L. & Schubert, G. *Geodynamics* (Cambridge Univ. Press, 2002).
73. Plank, T. & Forsyth, D. W. Thermal structure and melting conditions in the mantle beneath the Basin and Range province from seismology and petrology. *Geochem. Geophys. Geosyst.* **17**, 1312–1338 (2016).
74. Herzberg, C. & Asimow, P. D. Petrology of some oceanic island basalts: PRIMELT2.XLS software for primary magma calculation. *Geochem. Geophys. Geosyst.* <https://doi.org/10.1029/2008GC002057> (2008).
75. Dixon, J. E. & Clague, D. A. Volatiles in basaltic glasses from Loihi Seamount, Hawaii: evidence for a relatively dry plume component. *J. Petrol.* **42**, 627–654 (2001).
76. Zhang, H. L., Cottrell, E., Solheid, P. A., Kelley, K. A. & Hirschmann, M. M. Determination of  $\text{Fe}^{3+}/\Sigma\text{Fe}$  of XANES basaltic glass standards by Mössbauer spectroscopy and its application to the oxidation state of iron in MORB. *Chem. Geol.* **479**, 166–175 (2018).
77. Bell, D. R., Rossman, G. R., Maldener, J., Endisch, D. & Rauch, F. Hydroxide in olivine: a quantitative determination of the absolute amount and calibration of the IR spectrum. *J. Geophys. Res. Solid Earth* **108**, 2105 (2003).
78. Paterson, M. & Olgaard, D. Rock deformation tests to large shear strains in torsion. *J. Struct. Geol.* **22**, 1341–1358 (2000).
79. Rudge, J. F. The viscosities of partially molten materials undergoing diffusion creep. *J. Geophys. Res. Solid Earth* **123**, 10534–10562 (2018).
80. Becker, T. W. On the effect of temperature and strain-rate dependent viscosity on global mantle flow, net rotation, and plate-driving forces. *Geophys. J. Int.* **167**, 943–957 (2006).
81. Turner, A. J., Katz, R. F., Behn, M. D. & Keller, T. Magmatic focusing to mid-ocean ridges: the role of grain-size variability and non-Newtonian viscosity. *Geochem. Geophys. Geosyst.* **18**, 4342–4355 (2017).
82. Frederiksen, A. & Bostock, M. Modelling teleseismic waves in dipping anisotropic structures. *Geophys. J. Int.* **141**, 401–412 (2000).
83. Holtzman, B. K. & Kendall, J. M. Organized melt, seismic anisotropy, and plate boundary lubrication. *Geochem. Geophys. Geosyst.* **11**, Q0AB06 (2010).

## Acknowledgements

We thank E. Bozdag for providing the global adjoint tomography model GLAD-M25, B. Romanowicz for the attenuation model SEMUCB-UMQ, M. Behn for his global flow model, C. A. Dalton for assistance with Perple\_X and discussions about partial melting, Z. Ma for help with CRUST1.0 and S. P. Grand for discussions about paper structure. This work was supported by the US National Science Foundation grant EAR-1829401 received by K.M.F.

## Author contributions

J.H. initiated the project and conducted the data analysis, comparison and modelling in the paper. K.M.F. advised on the seismological aspects and overall conclusions of the paper. T.W.B. advised on the geodynamical modelling and seismology results. E.G. advised on its petrological components. G.H. advised on rheological modelling. Interpretation of the results reflects discussions among the authors. The manuscript was written by J.H. with contributions from K.M.F. and other authors.

## Competing interests

The authors declare no competing interests.

## Additional information

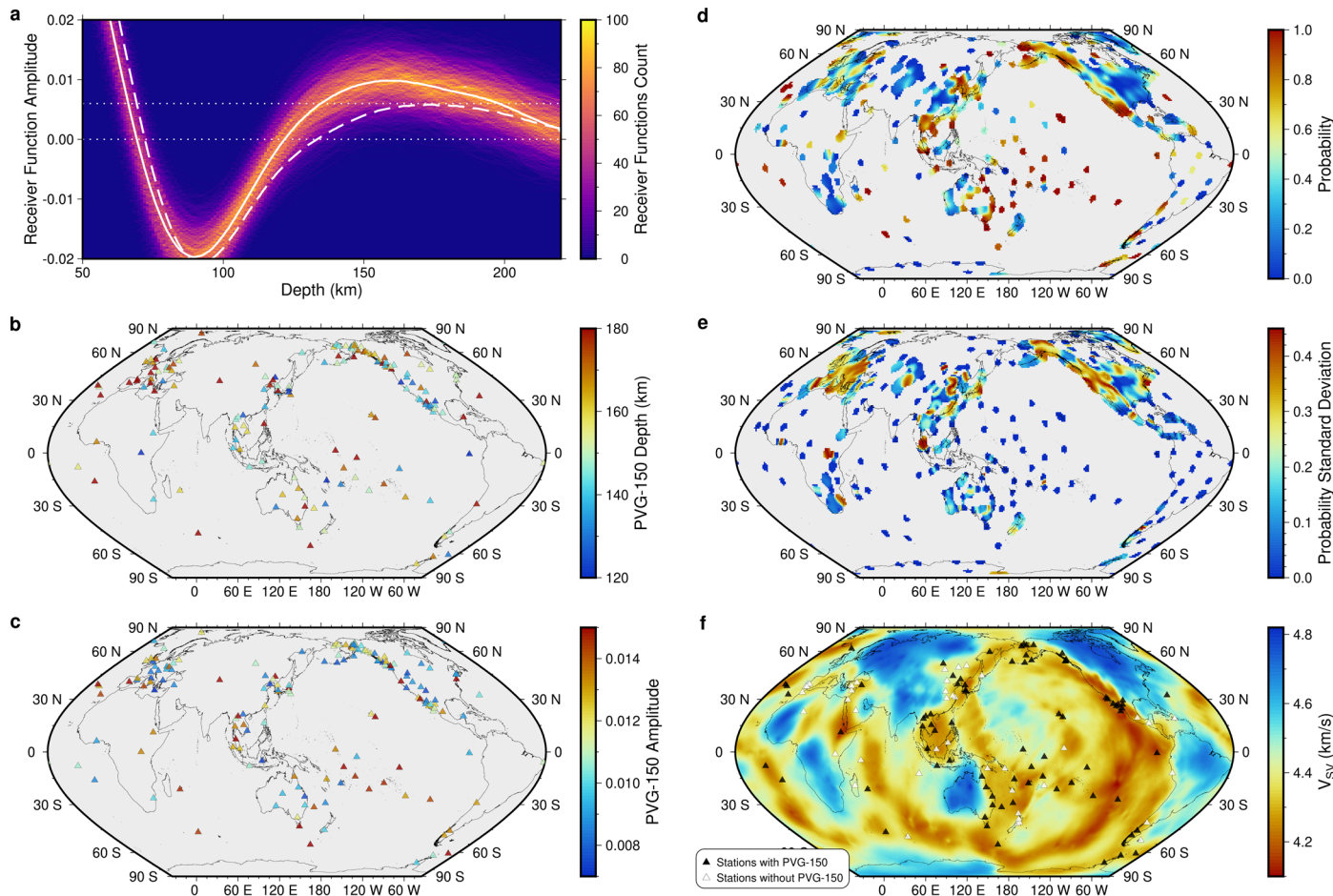
**Extended data** is available for this paper at <https://doi.org/10.1038/s41561-022-01116-9>.

**Supplementary information** The online version contains supplementary material available at <https://doi.org/10.1038/s41561-022-01116-9>.

**Correspondence and requests for materials** should be addressed to Junlin Hua.

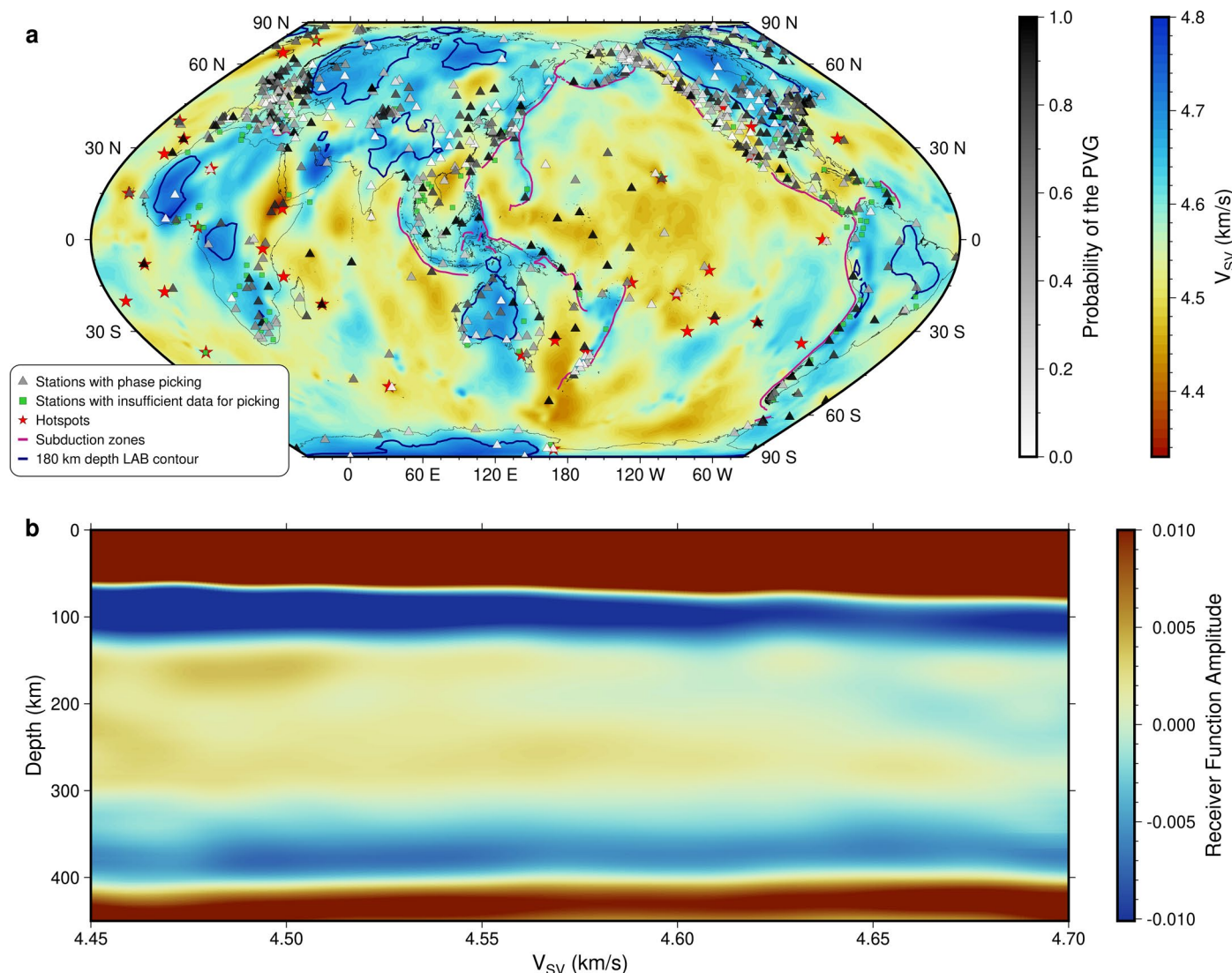
**Peer review information** *Nature Geoscience* thanks Geeth Manthilake, Mingming Jiang and the other, anonymous, reviewer(s) for their contribution to the peer review of this work. Primary Handling Editor: Louise Hawkins, in collaboration with the *Nature Geoscience* team.

**Reprints and permissions information** is available at [www.nature.com/reprints](http://www.nature.com/reprints).



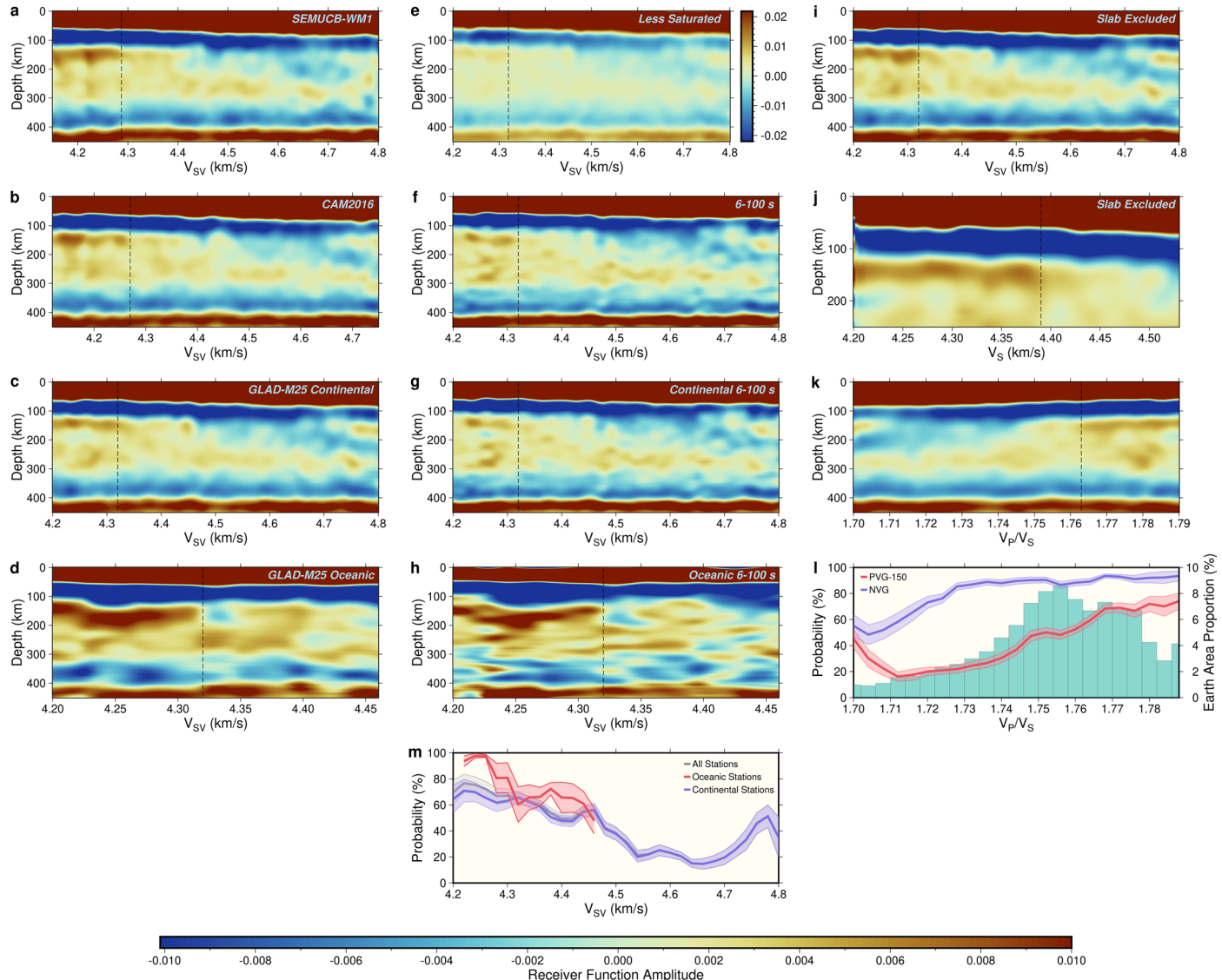
**Extended Data Fig. 1 | Probabilities of the PVG-150 phase.** **a.** Example of estimating the probability of the PVG-150 phase from the Sp receiver function at station SMAI (Antarctic Peninsula) in network AI. The solid line shows the receiver function amplitude. The background shows the heat map for the 3,000 perturbed receiver functions. The dashed line shows one of the perturbed receiver functions, whose maximum amplitude is below the threshold amplitude for picking of 0.006 (dotted line). In this case, no PVG-150 phase is picked, although the original stacked receiver function has an amplitude much higher than the threshold. Among all perturbed receiver functions, 96.9% produce a picked PVG-150 phase. The other dotted line shows zero amplitude. **b.** Map of the depth of the PVG-150 phase for those with probabilities over 0.8 (Fig. 1a). **c.**

Similar to **b** but for the maximum amplitude of the PVG-150 phase as defined in Extended Data Fig. 4d. **d.** Map of the probability of the PVG-150 phase obtained from weighted averaging of the probability at surrounding stations. **e.** Map of the uncertainty of the PVG-150 phase probability represented by the weighted standard deviation among surrounding stations. **f.** Stations (triangles) with similar PVG-150 phase probability relative to neighboring stations indicated by  $W_3$  (Eq. 4) values over 0.4. These stations have the strongest contributions to the average mantle profiles in Fig. 4a and Extended Data Fig. 8. Black triangles indicate stations with the PVG-150 (probability over 0.8), and white triangles show stations without the PVG-150 (probability below 0.2). Background shows average  $V_{sv}$  at 110–130 km depths<sup>22</sup>, as in Fig. 1a.



**Extended Data Fig. 2 | The PVG-260 phase.** **a.** Map similar to Fig. 1a, but in this case PVGs were picked between 230 and 350 km depths, which is the potential depth range for X-discontinuities<sup>25</sup>. The background  $V_{SV}$ <sup>22</sup> is at 260 km depth. Hotspots<sup>61–63</sup>, subduction zones<sup>64</sup> and the rim of cratons represented by the 180

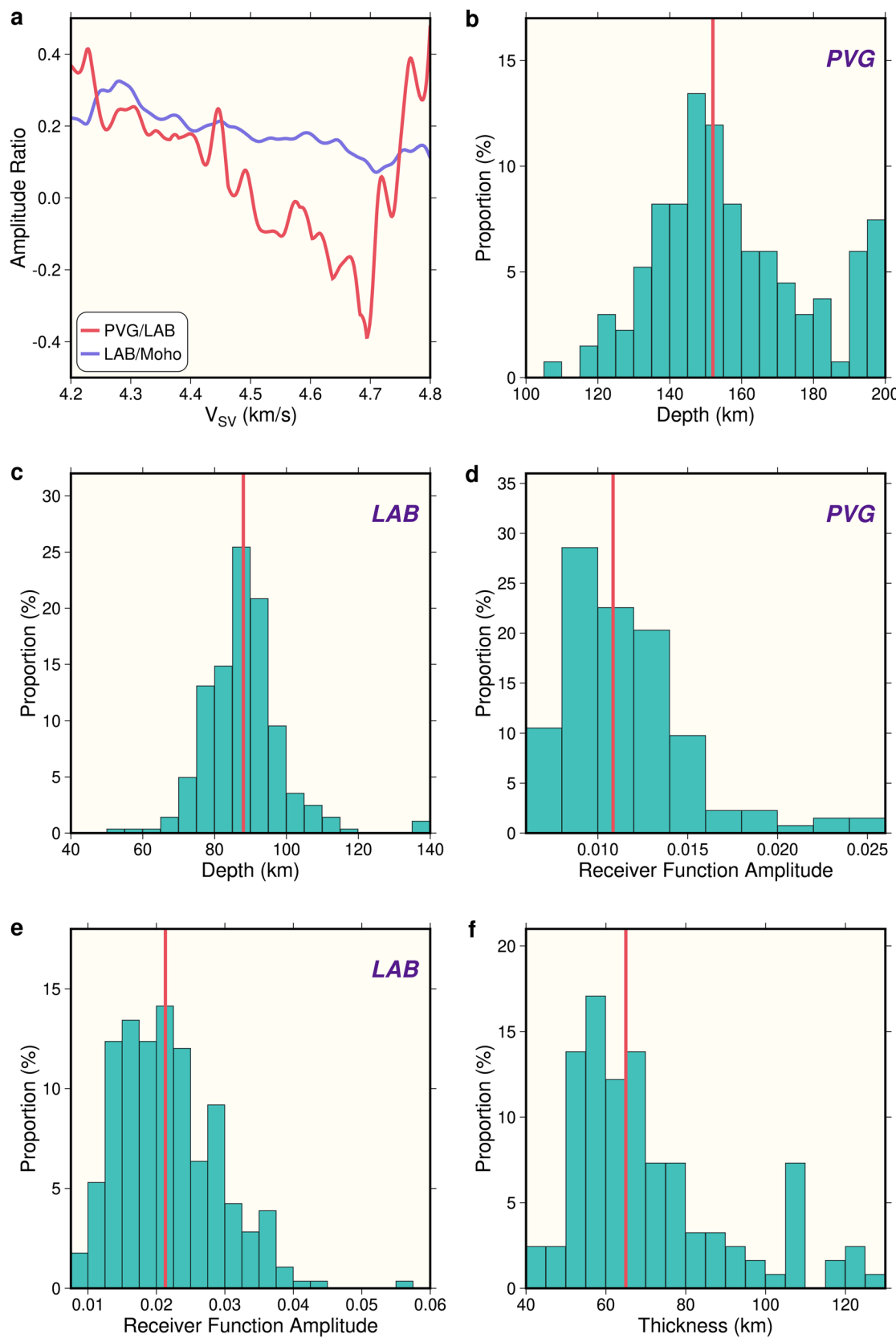
LAB contour in ref.<sup>2</sup> are also plotted. **b.** Observed receiver functions, similar to Fig. 2a, but binned by  $V_{SV}$  at 260 km depth. The PVG-260 phase is present across a wider range of  $V_{SV}$  values than the PVG-150.



**Extended Data Fig. 3 | Relationships between receiver functions and mantle properties.** a-b. Observed receiver functions binned by average  $V_{SV}$  at 110–130 km depths beneath the station, similar to Fig. 2a, but based on different reference velocity models: (a) SEMUCB-WM1 (ref. 21) (b) CAM2016 (ref. 2). (c-d) Similar to Fig. 2a, with the same reference model<sup>22</sup>, but using only the 644 continental stations (c) or only the 74 oceanic stations (d). A station was designated as oceanic if its crustal type in CRUST1.0 (ref. 65) is normal oceanic, oceans 3 Myr and younger, melt affected ocean and oceanic plateaus, or oceanic plateau with continental crust. e. The same as Fig. 2a, but with a less saturated color scale to show the NVG phase better. f-h. Similar to Fig. 2a and panels c and d, respectively, but filtered with a 6–100 s bandpass filter instead of 10–100 s.

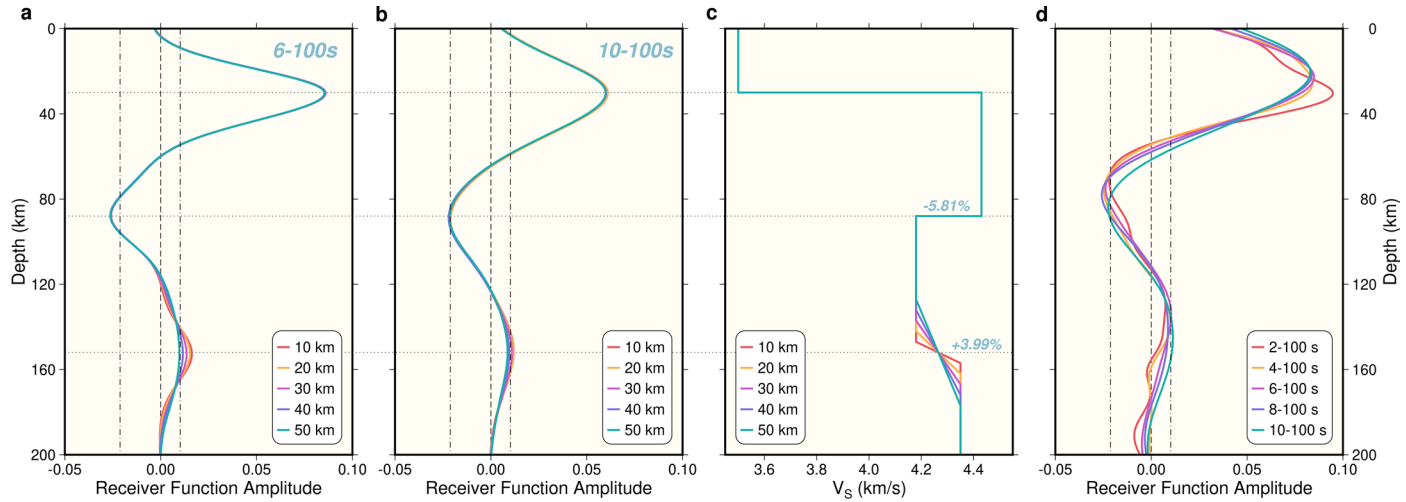
**i-j** Similar to Figs. 2a and 3c, respectively, but with stations close to subducting slabs removed. A station was designated as near a subducting slab if it is located within 1° of any slab depth that is shallower than 250 km based on Slab2 (ref. 66).

**k-l** Similar to Fig. 2a,b but plotted with respect to the average  $V_p/V_s$  at 110–130 km depths. m. Similar to Fig. 2b, but only with PVG-150 probabilities; Lines are for all stations combined, oceanic stations only, and continental stations only. The dashed lines in a-k mark the maximum (minimum for k) value with a clear PVG-150 phase; in c-i they are placed at the same  $V_{SV}$  as in Fig. 2a in j at the same  $V_s$  of 4.39 km/s as in Fig. 3c and in a, b and k at 4.29 km/s, 4.27 km/s and 1.763. The color bar at the bottom of the figure pertains to all panels except e, whose color bar is on its right side.


**Extended Data Fig. 4 | Properties of the PVG and NVG (LAB) phases.**

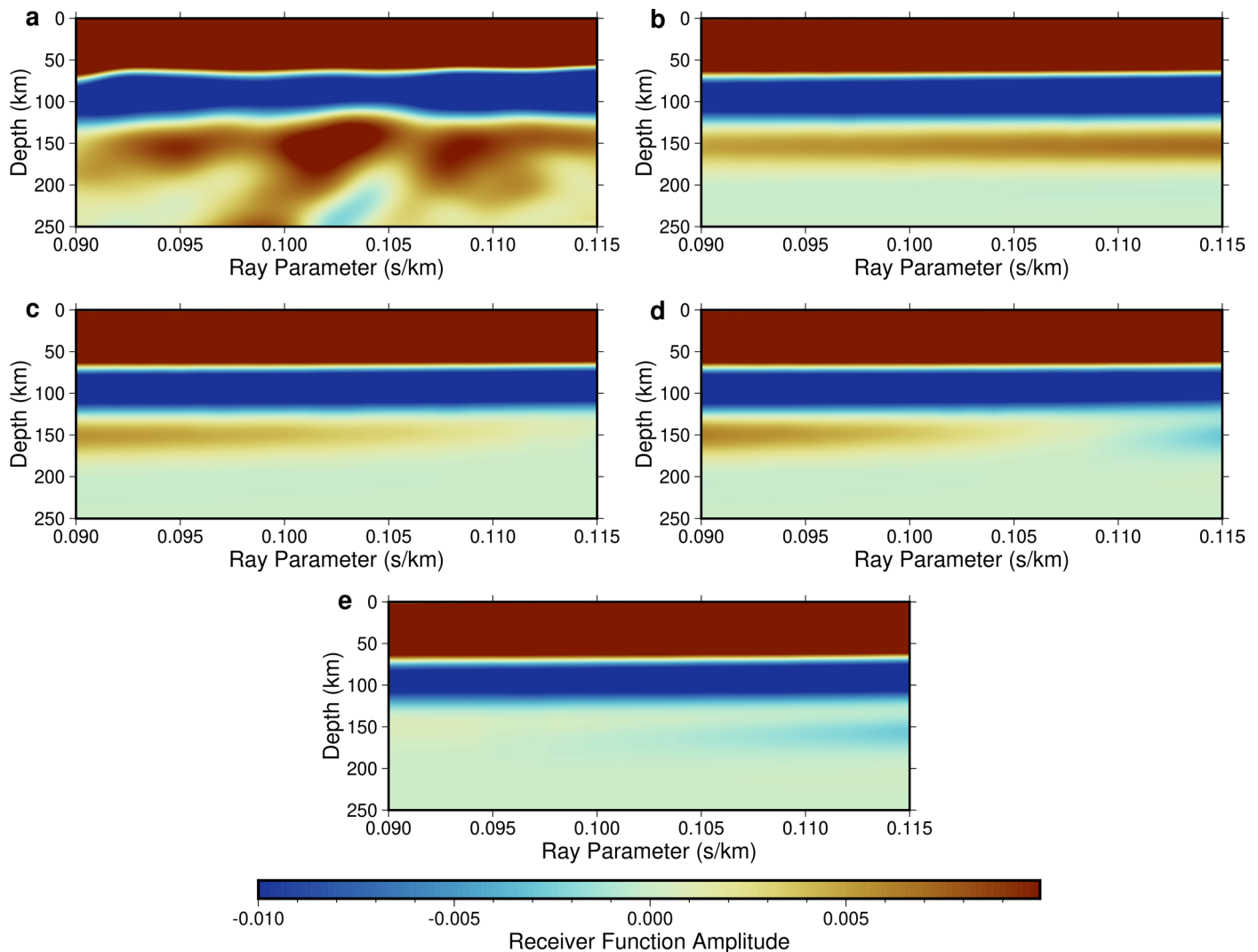
**a.** Amplitude ratios between PVG-150 and LAB phases, and between LAB and Moho phases as a function of average  $V_{SV}$  at 110–130 km depths<sup>22</sup>. The Moho amplitude is defined as the maximum receiver function amplitude above 80 km depth for each  $V_{SV}$ , the LAB amplitude is the maximum negative amplitude between 50 and 150 km depths, and the PVG-150 amplitude is the maximum value between 100

and 200 km depths in Fig. 2a. **b.** The distribution of picked PVG-150 depths. **c.** The distribution of picked LAB depths. **d.** The PVG-150 amplitude distribution. **e.** The LAB amplitude distribution. **f.** The distribution of LVZ thickness from stations with both PVG and LAB phase picks. Lines show the median values for the distributions. All the distributions are based on non-cratonic stations (defined as having average  $V_{SV}$  at 110–130 km depths below 4.46 km/s).



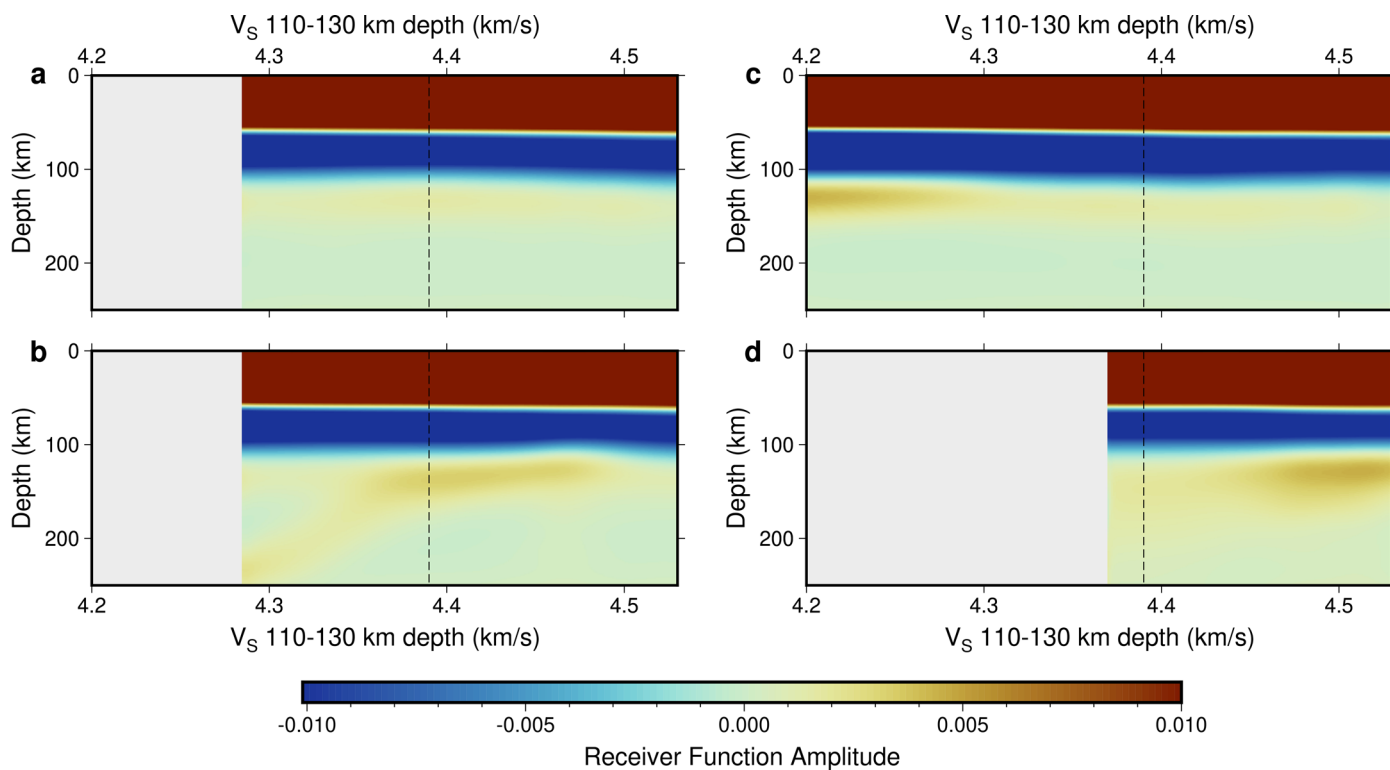
**Extended Data Fig. 5 | The effects of waveform frequency content.** Synthetic Sp receiver functions for the velocity models in **c** were filtered by 6–100 s (**a**) and 10–100 s (**b**) bandpass filters before deconvolution. Colors correspond to velocity gradients from the LVZ to the underlying asthenosphere over 10 to 50 km depth ranges (as shown in **c**). Horizontal dotted lines show the center of  $V_s$  discontinuities. Vertical dashed lines mark zero amplitude for receiver functions. The vertical dotted-dashed lines in **a** & **b** show the median NVG and PVG amplitudes (Extended Data Fig. 4) of the observed phases when filtered over 10–100 s. This analysis shows that the 10–100 s filter receiver functions are

less sensitive both to changes in the velocity gradient depth range and to small variations in the absolute depth of the velocity gradient. The 10–100 s filter was therefore chosen to measure globally-averaged PVG-150 properties. **d**) The effect of a range of filters on observed receiver function stacks at a single station (ANM, AK network), whose NVG and PVG amplitudes are close to the median of all stations (dashed lines). Colors correspond to receiver functions filtered over different period ranges. Filters containing shorter periods show greater separation between the LAB NVG and the PVG-150, providing additional evidence that the PVG-150 is not a side-lobe.



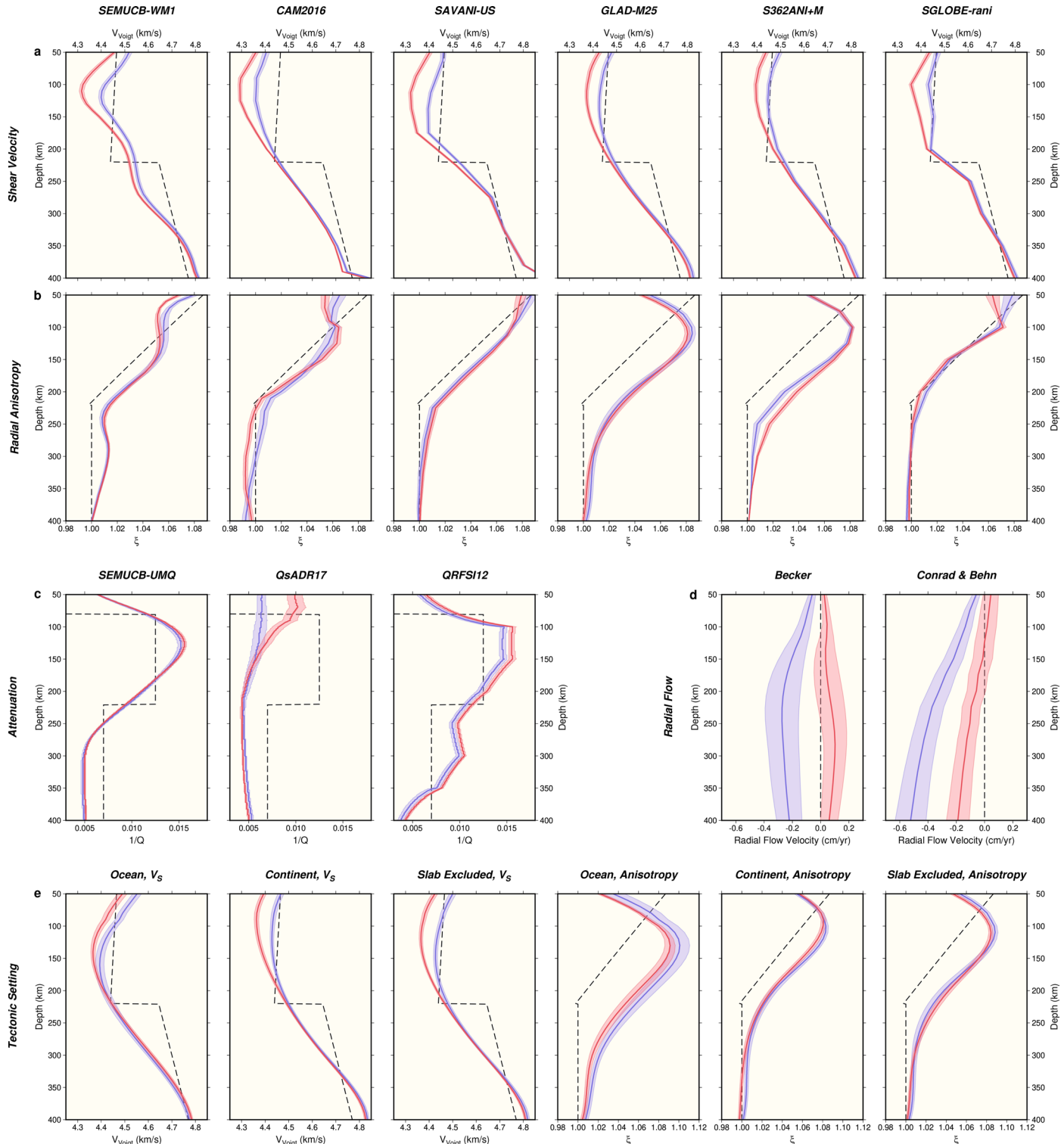
**Extended Data Fig. 6 | Ray parameter dependence of the Sp receiver functions.** **a.** Observed Sp receiver functions binned as a function of ray parameter. **b.** Synthetic Sp receiver functions for a mantle with an isotropic LVZ (LVZ  $V_s$  lower than the underlying mantle). **c.** Synthetic Sp receiver functions where the LVZ is radially anisotropic with  $\xi$  equal to 1.1 but has no P anisotropy, and its  $V_{\text{Voigt}}$  is the same as the underlying mantle. **d.** The LVZ contains P

anisotropy ( $\varphi^{-1} = V_{\text{PH}}^2/V_{\text{PV}}^2$  is 0.96) but no S anisotropy, and its Voigt average for P-wave velocity is the same as the underlying mantle. **e.** The LVZ contains both S ( $\xi$  equal to 1.1) and P anisotropy ( $\varphi^{-1}$  equal to 1.04, the value suggested by PREM<sup>27</sup> when  $\xi$  is 1.1), and the Voigt average for S-wave and P-wave velocities are the same as the underlying mantle. All anisotropic layers in **c-e** have an  $\eta$  of 0.9, consistent with PREM<sup>27</sup> when  $\xi$  is 1.1.



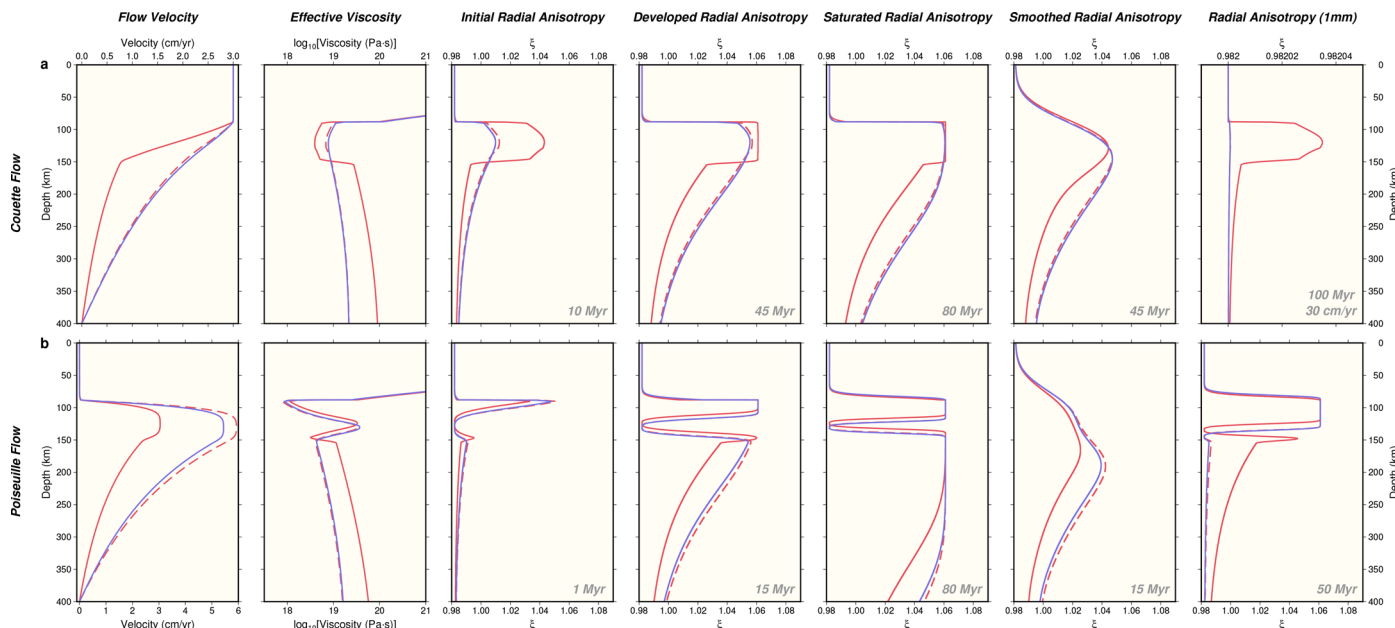
**Extended Data Fig. 7 | Binned synthetic receiver functions.** **a.** Predicted receiver functions similar to Fig. 3b, but produced from velocities that are those in Fig. 3a minus the poroelasticity effect of partial melt<sup>33</sup>. **b.** Similar to a, but velocities also include the effects of a small amount of melt on diffusion

creep viscosity<sup>10</sup> which strongly influences anelasticity where melting occurs. **c.** Similar to Fig. 3b, but with a grain size of 1 mm (10 mm for Fig. 3b). **d.** Similar to a, but the anelasticity is based on ref. <sup>67</sup> to include pre-melting effects, and the poroelasticity effect is not included. Black dashed lines are the same as in Fig. 3.



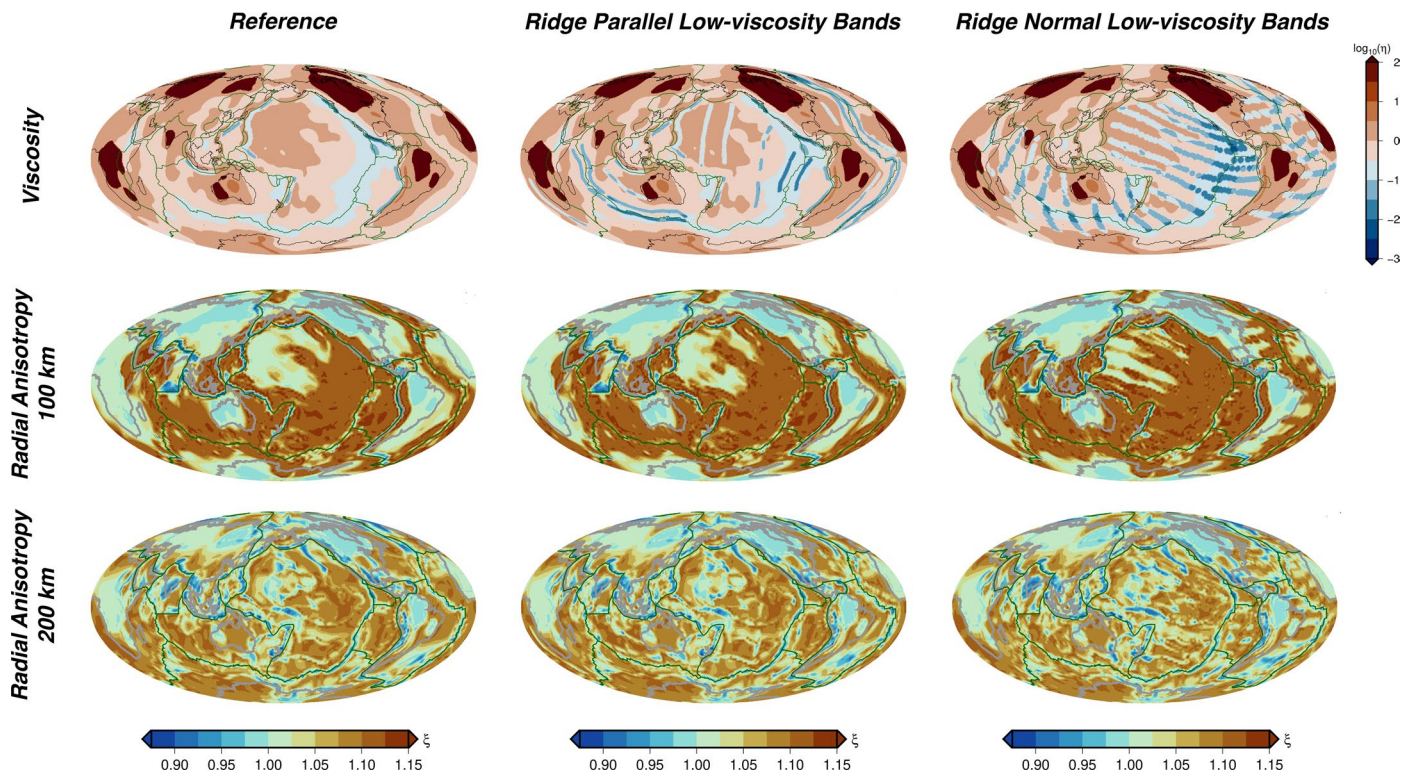
**Extended Data Fig. 8 | Mantle property contrasts between areas with and without the PVG-150 phase.** The first three rows show differences in weighted averaged (Eq. 4) profiles of  $V_{\text{Voigt}}$  (a),  $\xi$  (b), attenuation (c) and radial mantle flow velocity (d) for stations with (red lines) and without (blue lines) the PVG-150 phase. The fourth row (e) shows differences in weighted averaged profiles of  $V_{\text{Voigt}}$  and  $\xi$  for different tectonic settings. Transparent areas show one standard deviation for the averaged profiles. Black dashed lines are reference values from PREM<sup>27</sup>. For  $V_{\text{Voigt}}$  and  $\xi$ , columns are for velocity models SEMUCB-WM1 (ref. <sup>21</sup>),

CAM2016 (refs. <sup>2,40</sup>), SAVANI-US<sup>42</sup>, GLAD-M25 (ref. <sup>22</sup>), S362ANI + M<sup>41</sup> and SGLOBE-rani<sup>39</sup>. For attenuation, columns show models SEMUCB-UMQ<sup>59</sup>, QsADR17 (ref. <sup>60</sup>) and QRFSI12 (ref. <sup>58</sup>). For radial mantle flow velocity, the first column contains modeled radial flow velocity based on the approach in ref. <sup>43</sup> and the tomographic model in ref. <sup>68</sup>, and the second column shows the modeled velocity from ref. <sup>69</sup>. For tectonic settings<sup>70–83</sup>, we considered oceanic regions, continental regions, and regions excluding subducting slabs; these tectonic groups are defined the same as in Extended Data Fig. 3.


**Extended Data Fig. 9 | 1D modeling of radial anisotropy assuming different effects of partial melt.**

**Effects of partial melt.** First and second rows illustrate the 1D models of mantle Couette (a) and Poiseuille flow (b) (1,450 °C cases). The first column shows the solution for mantle flow velocity, and the second column is the equivalent mantle viscosity. The 3<sup>rd</sup> to 5<sup>th</sup> columns show predicted  $\xi$  for different points in time: early in strain accumulation; when radial anisotropy has developed to resemble the observed profiles; and when anisotropy has reached its saturation level over a broad depth range. The time intervals of strain accumulation for these three stages are labelled in the bottom right corners. The sixth column shows the product of the fourth column convolved with a Gaussian whose standard

deviation is 30 km to mimic the potential for reduced vertical resolution in tomography due to broad surface wave sensitivity kernels. The seventh column shows the radial anisotropy when grain size is 1 mm (10 mm for other columns); here the plate motion for Couette flow is set to 10 cm/yr (with a different x-axis), and the longer deformation times are labeled. Same as in Fig. 4b, blue lines are for the case when the effects of partial melt on viscosity are ignored; red dashed lines show when partial melt effects are only characterized by a moderate exponential term<sup>34</sup>; and red solid lines are the case when a factor of 5 viscosity increase is introduced across 150 km depth to represent stronger partial melting impacts on viscosity above the PVG-150.



**Extended Data Fig. 10 | Modelled 3D radial anisotropy with localized asthenospheric viscosity layering.** Model results in this figure are all from ref. <sup>43</sup>. The first row shows the relative mantle viscosity at 134 km depth, and in the corresponding second and third columns, low-viscosity bands parallel or perpendicular to the mid-ocean ridges are present at depths between 100 and

150 km. Beneath 150 km depth, the reference viscosity distribution (first column) is assumed. The second and third rows show predicted  $\xi$  structures at 100 and 200 km depths for viscosity structures in the first row. At 100 km depth, radial anisotropy is increased in the low viscosity bands, and at 200 km depth, radial anisotropy is decreased beneath the low viscosity bands.